The Astrophysical Journal Supplement Series, 247:28 (20pp), 2020 March https://doi.org/10.3847/1538-4365/ab7230

Scaling *K2*. I. Revised Parameters for 222,088 *K2* Stars and a *K2* Planet Radius Valley at 1.9 $R_\oplus$

Kevin K. Hardegree-Ullman[1], Jon K. Zink[1,2], Jessie L. Christiansen[1], Courtney D. Dressing[3], David R. Ciardi[1], and Joshua E. Schlieder[4]
[1] Caltech/IPAC-NASA Exoplanet Science Institute, Pasadena, CA 91125, USA; kevinkhu@caltech.edu
[2] Department of Physics and Astronomy, University of California, Los Angeles, CA 90095, USA
[3] Astronomy Department, University of California, Berkeley, CA 94720, USA
[4] Exoplanets and Stellar Astrophysics Laboratory, Code 667, NASA Goddard Space Flight Center, Greenbelt, MD 20771, USA
Received 2019 October 7; revised 2020 January 29; accepted 2020 January 30; published 2020 March 10

Abstract

Previous measurements of stellar properties for *K2* stars in the Ecliptic Plane Input Catalog largely relied on photometry and proper motion measurements, with some added information from available spectra and parallaxes. Combining *Gaia* DR2 distances with spectroscopic measurements of effective temperatures, surface gravities, and metallicities from the Large Sky Area Multi-Object Fibre Spectroscopic Telescope (LAMOST) DR5, we computed updated stellar radii and masses for 26,838 *K2* stars. For 195,250 targets without a LAMOST spectrum, we derived stellar parameters using random forest regression on photometric colors trained on the LAMOST sample. In total, we measured spectral types, effective temperatures, surface gravities, metallicities, radii, and masses for 222,088 A, F, G, K, and M-type *K2* stars. With these new stellar radii, we performed a simple reanalysis of 299 confirmed and 517 candidate *K2* planet radii from Campaigns 1–13, elucidating a distinct planet radius valley around 1.9 $R_\oplus$, a feature thus far only conclusively identified with *Kepler* planets, and tentatively identified with *K2* planets. These updated stellar parameters are a crucial step in the process toward computing *K2* planet occurrence rates.

Unified Astronomy Thesaurus concepts: Fundamental parameters of stars (555); Exoplanet systems (484); Exoplanets (498)

Supporting material: machine-readable tables

1. Introduction

The ubiquity of exoplanets in the Galaxy has been established by NASA's *Kepler* Telescope (Borucki et al. 2010), with the discovery of thousands of confirmed and candidate planets[5] in both the *Kepler* prime and subsequent *K2* missions. After the failure of two reaction wheels on *Kepler*, the *K2* mission was commissioned, which allowed the *Kepler* spacecraft to stare at different fields along the ecliptic plane for approximately 80 days at a time, using radiation pressure from the Sun to act as a third stabilization axis (Howell et al. 2014).

Our knowledge of the hundreds of confirmed and candidate planets discovered in the *K2* data relies on accurate and precise stellar radius measurements for their host stars. In large surveys of hundreds of thousands of stars, like *K2*, it is practical to rely on stellar properties derived from readily available data. The values for *K2* targets in the Ecliptic Planet Input Catalog (EPIC) come from Huber et al. (2016); they were measured with `galclassify`,[6] which uses the *Galaxia* synthetic Milky Way model (Sharma et al. 2011) and the Padova isochrones (Girardi et al. 2000; Marigo & Girardi 2007; Marigo et al. 2008). The input sources to `galclassify` were reduced proper motions, spectra from the Large Sky Area Multi-Object Fiber Spectroscopic Telescope DR1 (LAMOST; Luo et al. 2015), the Radial Velocity Experiment DR4 (RAVE; Kordopatis et al. 2013), and Apache Point Observatory Galactic Evolution Experiment DR12 (APOGEE; Alam et al. 2015), parallax measurements from *Hipparcos* (van Leeuwen 2007), and photometric measurements from the US Naval Observatory CCD Astrograph Catalog (UCAC4; Zacharias et al. 2013), the Sloan Digital Sky Survey (SDSS; Skrutskie et al. 2006), and the Two Micron All Sky Survey (2MASS; Skrutskie et al. 2006). For *K2* Campaigns 1–8, 81% of the stars were characterized using colors and reduced proper motions, 11% from colors only, 7% from spectroscopy, and 1% from parallaxes and colors (Huber et al. 2016).

Since the EPIC was released, the European Space Agency's *Gaia* mission (Gaia Collaboration et al. 2016) has now measured parallaxes for over 1.3 billion sources in DR2 (Gaia Collaboration et al. 2018). Subsequently, Berger et al. (2018) revised the radii of *Kepler* stars and planets, reducing typical uncertainties on those measurements by a factor of 4–5 in most cases. Measurements of stellar parameters in the EPIC were largely based on photometry and proper motions, which can introduce biases in derived properties like temperature and surface gravity. Huber et al. (2016) noted specifically for subgiants that 55–70% were misclassified as dwarf stars. Consequently, stellar properties for these stars had large uncertainties. Since the different *K2* fields span a wide range of galactic latitudes, these biases are potentially caused by poor measurements of interstellar extinction. Additionally, the Padova isochrones are known to underestimate the radii of cool stars (Boyajian et al. 2012), and Huber et al. (2016) caution that EPIC M dwarf radii can be underestimated by up to 20%. The exquisite precision of the *Gaia* measurements, improved interstellar extinction maps such as those from Green et al. (2018), and recent empirical calibrations for cool stars (Mann et al. 2015, 2019), allow us to better constrain absolute magnitudes and refine stellar parameters based on photometry.

A moderate-resolution stellar spectrum can be used to constrain basic stellar parameters more precisely than

[5] https://exoplanetarchive.ipac.caltech.edu/docs/counts_detail.html
[6] https://github.com/danxhuber/galclassify

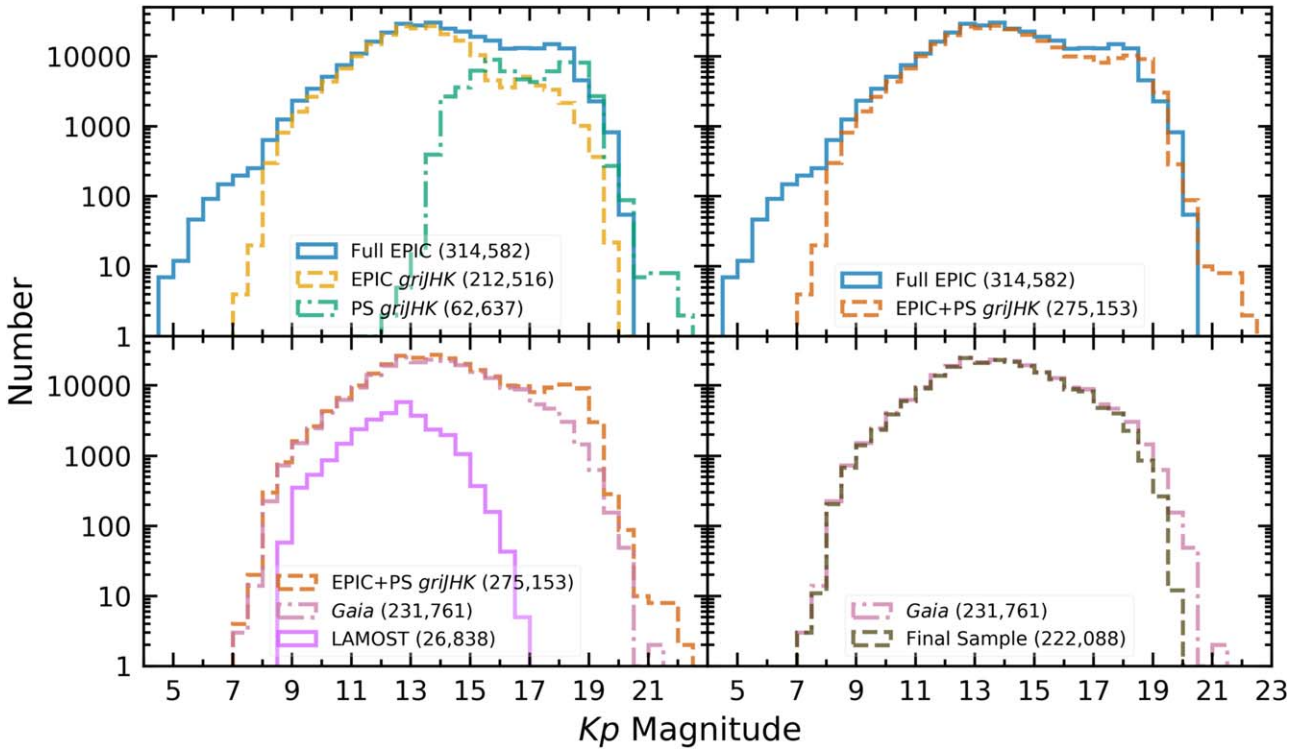

Figure 1. Magnitude distributions highlight each of our sample cuts. Upper left: the full EPIC catalog (solid), EPIC targets with full optical and 2MASS infrared photometry (dashed), and additional *K2* targets with Pan-STARRS and 2MASS photometry (dashed–dotted). *Kp*-band magnitudes were recomputed for *K2* targets with Pan-STARRS photometry, which is why there are a few targets fainter than the original EPIC catalog. Upper right: the full EPIC catalog (solid) and the combined EPIC and Pan-STARRS targets (dashed). Lower left: the combined EPIC and Pan-STARRS targets (dashed), *K2* targets with a *Gaia* parallax (dashed–dotted), and targets with a LAMOST spectrum (solid). *Gaia* is nearly complete between $G = 12$ and $G = 17$ (Gaia Collaboration et al. 2018), which explains why *Gaia* targets diminish beyond $Kp \approx 17$. Understandably, targets with a LAMOST spectrum are relatively bright due to our S/N cuts. Lower right: The *Gaia* (dashed–dotted) and final target samples (dashed). Our color cuts mostly removed the faintest targets from our final sample.

photometry alone, such as spectral type, effective temperature ($T_{\rm eff}$), surface gravity ($\log g$), and metallicity, which is commonly measured as iron abundance [Fe/H]. For transiting exoplanet studies, planet radius measurements are limited by the precision to which we know the radius of their host star. With bolometric luminosities and effective temperatures, we can measure stellar radii ($R_\star$) from the Stefan–Boltzmann law. If surface gravity is also constrained, then a stellar mass ($M_\star$) can also be measured, which is necessary for constraining planet masses from radial velocities.

Several catalogs of *K2* planets have gathered spectra of planet candidate host stars (e.g., Crossfield et al. 2016; Dressing et al. 2017a, 2017b, 2019; Martinez et al. 2017; Mayo et al. 2018; Petigura et al. 2018). Different instruments and analysis techniques, however, produce different results, necessitating cross calibration between catalogs if conclusions are to be drawn about planet populations across the *K2* campaigns. Stars without known or candidate planets are often overlooked for spectroscopic stellar characterization. This information is needed for accurate studies of planet occurrence rate calculations by spectral type, and drawing conclusions about planet host and non-host populations. Of course, photometry is much more readily available than spectroscopy for most stars, but large spectroscopic surveys such as LAMOST, RAVE, and APOGEE provide a wealth of information for millions of stars that are unbiased toward planet hosts.

Precise stellar radii for planet hosts can also reveal information about underlying planet populations. Indeed, one of the key results from the *Kepler* mission was the discovery of a planet radius valley between ~1.5 and 2.0 Earth radii ($R_\oplus$) by Fulton et al. (2017), which was enabled by improved precision in stellar radius measurements from California–*Kepler* Survey spectra. This planet radius gap was independently observed using a smaller set of *Kepler* targets with stellar properties measured from asteroseismology (Van Eylen et al. 2018). The astrophysical origin of this effect has been explored by Owen & Wu (2013), Lee et al. (2014), Lee & Chiang (2016), Owen & Wu (2017), and Lopez & Rice (2018). Using *K2* data, Mayo et al. (2018) and Kruse et al. (2019) both identified a "tentative" planet radius gap with their catalogs of 275 planet candidates from Campaigns 0–10 and 818 planet candidates from Campaigns 0–8, respectively. Mayo et al. (2018) computed stellar radii using `isochrones` (Morton 2015), with inputs of effective temperature, surface gravity, and metallicity derived from high-resolution ($R \approx 44{,}000$) Tillinghast Reflector Echelle Spectrograph optical spectra (5059–5317 Å). They compared their planet radius distribution to the Fulton et al. (2017) distribution, but found that a log-uniform distribution fit their data equally well, which they attribute to their relatively small planet sample. Kruse et al. (2019) used stellar radii from *Gaia* for 648 of their targets and from the EPIC for most of the remaining stars without a *Gaia* measurement. They also conservatively call their planet radius gap tentative due to planet radius uncertainties and a limited sample.

In this paper, we leverage parallaxes from *Gaia*, stellar properties from LAMOST spectra, and photometry from the EPIC to calculate revised stellar properties (spectral type, distance, $T_{\rm eff}$, $\log g$, [Fe/H], $R_\star$, and $M_\star$) for 222,088 *K2* stars. In Section 2, we update target photometry and describe our target selection criteria from the EPIC, *Gaia*, and LAMOST. For stars with both a *Gaia* parallax and a LAMOST spectrum, we describe our spectroscopic stellar classification for A, F, G,

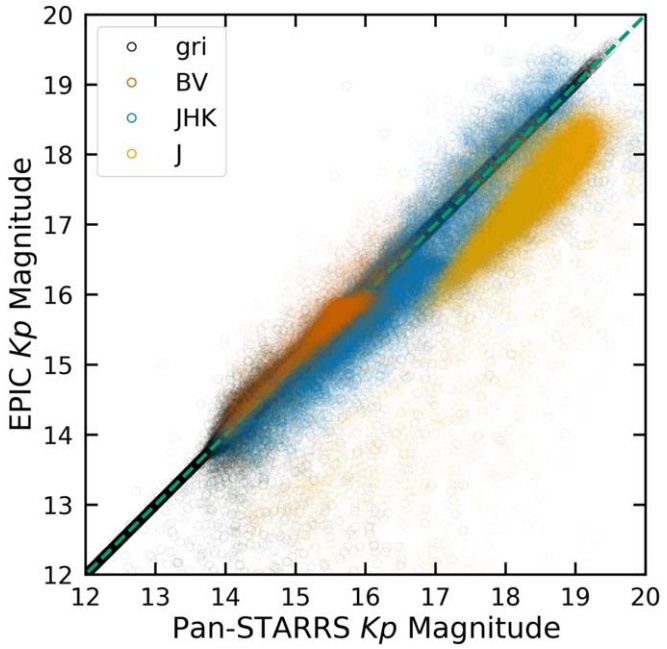

Figure 2. Comparison of *Kp* magnitudes computed using Pan-STARRS *g*, *r*, and *i*-band photometry to previous measurements with optical (gri, black; BV, red) and infrared (JHK, blue; J, orange) photometry. Optical magnitude estimates are very similar. Previous measurements of *Kp* from JHK photometry are skewed toward overestimating brightness. Previous *J*-band *Kp* magnitude estimates are on average one magnitude brighter than our new optical measurements. The apparent truncation of Pan-STARRS *Kp* measurements brighter than ∼14th magnitude for targets with previous estimates from BV, JHK, and *J*-band photometry is due to the Pan-STARRS saturation limit of $g \lesssim 14.5$. For targets with Pan-STARRS measurements brighter than the saturation limit, we instead used EPIC gri photometry when available. We truncate the plot at 12th magnitude to highlight computed *Kp* differences, and because brighter targets follow the one-to-one line (gray dashed).

and K (AFGK) type stars in Section 3, and M dwarfs in Section 4. We compute stellar properties for the remaining stars with only *Gaia* parallaxes and photometry in Section 5. In Section 6, we compare our revised stellar parameters to the EPIC, and remeasure *K2* planet radii which we use to identify a clear *K2* planet radius valley at 1.9 $R_\oplus$.

2. Catalog

We started with the *K2* observed target catalog,[7] which contains 342,964 targets with an object type of "star." Several targets were observed in multiple campaigns, in which case we remove duplicate EPIC IDs, leaving us with 314,582 unique targets. Of these unique targets, there are 212,516 with UCAC4 or SDSS *g*, *r*, and *i*-band, and 2MASS *J*, *H*, and K_s-band photometry, which we use later for target selection and stellar classification. Figure 1 shows *Kepler Kp*-band magnitude distributions from the full EPIC catalog along with distributions from each of our target sample cuts, which we discuss in the following sections.

2.1. Panoramic Survey Telescope and Rapid Response System (Pan-STARRS) Photometry

There are 87,828 targets with complete *J*, *H*, and K_s-band photometry but incomplete or missing *g*, *r*, and *i*-band photometry. Using the EPIC IDs for these targets, we queried the Pan-STARRS (Chambers et al. 2016) DR2 database (Flewelling et al. 2016). This resulted in *g*, *r*, and *i*-band photometry (mean PSF magnitudes) for 62,637 targets. These targets are on average between 2 and 2.5 magnitudes fainter than the EPIC targets with previous *g*, *r*, and *i*-band photometry (Figure 1), which is likely why they did not have previous optical measurements.

The average Pan-STARRS photometric uncertainties are about 10 times smaller than the average EPIC photometric uncertainties in the *g* and *r*bands, and comparable in the *i*band. Thus, we queried the Pan-STARRS database for all EPIC targets with previous optical measurements, resulting in 84,176 additional Pan-STARRS measurements. We use Pan-STARRS photometry for any of our targets fainter than the saturation limit ($g \lesssim 14.5$[8]; 123,819 targets), and the EPIC values otherwise. In total, we have 275,153 unique targets with complete *g*, *r*, *i*, *J*, *H*, and K_s-band photometry (Figure 1).

We recomputed the *Kepler Kp* magnitude for all targets using our updated *g*, *r*, and *i*-band photometry and the following equations from Brown et al. (2011):

$$Kp = 0.25g + 0.75r, (g - r) \leqslant 0.3 \quad (1a)$$

$$Kp = 0.3g + 0.7i, (g - r) > 0.3 \quad (1b)$$

Previous measurements of *Kp* magnitudes were computed with less precise relationships from Brown et al. (2011) and Howell et al. (2012) using *B*, *V*, *J*, *H*, and K_s photometry if *g*, *r*, and *i*-band photometry was unavailable (Huber et al. 2016). The *Kepler Kp* filter response function (≳20% transmission 4300–8900 Å[9]) overlaps with the *g*, *r*, and *i*bands, so estimated magnitudes from these bands takes priority. We compared the newly computed *Kp* magnitudes to previous estimates in Figure 2. Estimates from *J*-band photometry alone tend to yield *Kp* measurements one magnitude brighter than from optical photometry.

2.2. Gaia

We used the *Gaia*/*K2* cross-match database[10] to obtain distances to our *K2* stars from Bailer-Jones et al. (2018). The 4″ radius cross-match between the aforementioned *K2* observed star catalog and the *Gaia* DR2 catalog yields 361,488 *Gaia*/*K2* entries and 294,114 unique EPIC IDs. We combined this cross-match table with our photometry table, reducing the *Gaia*/*K2* cross-match sample to 256,990 *Gaia* sources within 4″ of our 275,153 *K2* targets. The *K2* targets without a *Gaia* cross-match are on average ∼2.5 magnitudes fainter ($Kp = 16.38$) than those with a cross-match ($Kp = 13.85$), and about 60% of these targets are likely giant stars (based on $J - K$ versus $r - J$ colors; Muirhead et al. 2015).

The similarities between the *Gaia* *G*band (≳20% transmission 4000–9000 Å; Evans et al. 2018) and *Kepler Kp*band helped us to identify our *K2* target in the *Gaia* data in the case of multiple cross-matches, which could be a binary companion or background source. There are 212,376 *K2* targets with a single *Gaia* cross-match within 4″, 21,075 *K2* targets with more than one cross-match, and 41,702 without any *Gaia*

[7] https://exoplanetarchive.ipac.caltech.edu/cgi-bin/TblView/nph-tblView?app=ExoTbls&config=k2targets

[8] https://outerspace.stsci.edu/display/PANSTARRS/PS1+FAQ+-+Frequently+asked+questions

[9] https://keplergo.arc.nasa.gov/CalibrationResponse.shtml

[10] http://gaia-kepler.fun/

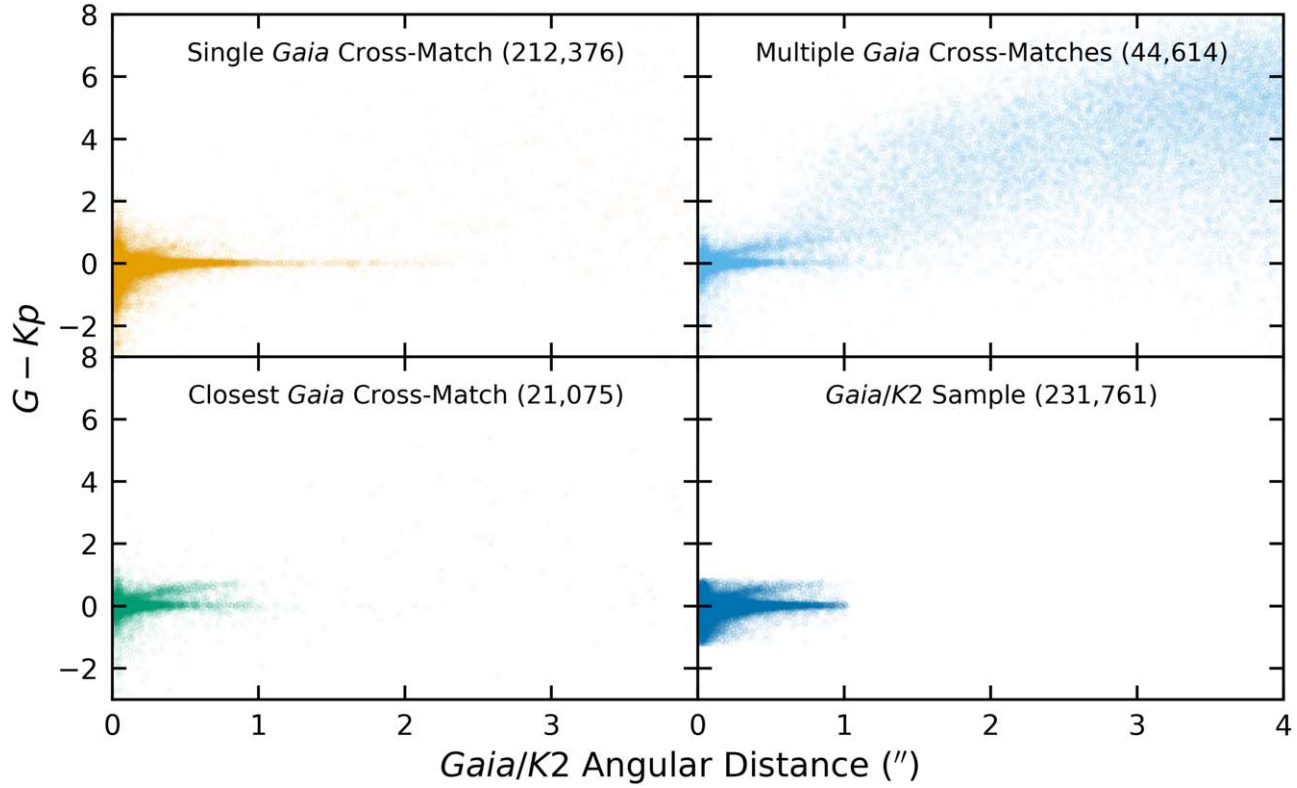

Figure 3. $G - Kp$ vs. $K2/Gaia$ angular distance for single *Gaia* cross-match sources (upper left) and multiple *Gaia* cross-matches (upper right). For the sources with multiple cross-matches, we selected the target with the closest distance to the origin, which effectively removed the multiple cross-match cloud (lower left). For the final sample, we selected targets within 3σ of the average angular distance and $G - Kp$ (lower right).

matches. There are a total of 44,614 different *Gaia* IDs for the 21,075 *K2* targets with more than one cross-match.

We plot $G - Kp$ versus $K2/Gaia$ angular distance in Figure 3 for both single and multiple cross-matches. If there were multiple cross-matches, we selected the target closest to the origin in $G - Kp$ and angular distance space (21,075 targets). For the multiple cross-matches, the distribution roughly follows that of single cross-match targets, but with a distinct branch extending into a cloud of sources with $G - \mathrm{Kp} \gtrsim 0$ and angular distance $\gtrsim 0\farcs75$. A simple investigation of targets along the extra branch in the closest *Gaia* cross-match plot does not indicate that these stars are distinct from the other closest match stars (e.g., common proper motion binary versus background star). Further analysis of this feature is encouraged, but is beyond the scope of this work. For quality control, we selected targets from the single and closest *Gaia* cross-match lists within 3σ of the average angular distance ($\sim 1''$) and $|G - Kp|$ (~ 1), leaving 231,761 unique targets (Figure 1).

2.3. LAMOST Spectra

LAMOST has a 4,000 fiber multi-object spectrograph (3690–9100 Å, $R \approx 1800$) to survey stars and galaxies in the northern hemisphere (Cui et al. 2012). LAMOST DR5 v3 contains over nine million[11] spectra. The LAMOST DR5 AFGK type star catalog[12] is comprised of 5,348,712 spectra across all evolutionary stages, and the M dwarf catalog contains 534,393 spectra. We chose to use only LAMOST spectra because it contains more spectra than either APOGEE or RAVE. This also mitigated any effects from cross-calibrating spectroscopic parameters from other surveys.

We selected AFGK spectra with signal-to-noise ratio (S/N) > 50 in the *g* and *r* bands, and M spectra with S/N > 50 in the *r* and *i* bands. Additionally, for comparison to our *K2* catalog, we required that the LAMOST targets also have associated *g*, *r*, and *i*-band photometry. Thousands of targets, as identified by their 2MASS designation, were observed more than once, in which case we kept the target with the highest S/N in the *r* band. This left us with 1,440,423 AFGK and 50,158 M star spectra with a unique 2MASS designation.

We used the Centre de Donnes astronomiques de Strasbourg (CDS) cross-match service[13] to cross-match our $Gaia/K2$ and LAMOST catalogs using a $4''$ search radius, yielding 29,134 AFGK and 1737 M star matches. To ensure we matched the correct target, we checked that the absolute difference between *g*, *r*, and *i* magnitudes in the LAMOST and EPIC catalogs were less than 0.15, a conservative 2σ from the median difference in each band. This left us with 25,450 AFGK and 1388 M stars that are *K2* targets with a LAMOST spectrum and *Gaia* parallax (Figure 1). For these targets, we computed absolute magnitudes for the *g*, *r*, *i*, *J*, *H*, and K_s-band photometry from the EPIC catalog (Table 1), accounting for interstellar extinction using `dustmaps` (Green et al. 2018).

The LAMOST pipeline (Luo et al. 2012, 2015) assigns a Morgan–Keenan spectral type to each spectrum. For the AFGK catalog, $T_{\rm eff}$, log *g*, and [Fe/H] were determined from the LAMOST stellar parameters pipeline (Wu et al. 2011), which

[11] http://dr5.lamost.org/
[12] http://dr5.lamost.org/catalog
[13] http://cdsxmatch.u-strasbg.fr/xmatch

Table 1
K2 Stellar Parameters

EPIC ID	*K2* Campaign	Pan-STARRS ID	*Gaia* DR2 ID	LAMOST ID	m_g (mag)	⋯
201048855	10	⋯	3582456140266586240	⋯	12.320 ± 0.040	
201049999	10	⋯	3582457617736883840	⋯	13.353 ± 0.030	
201050049	10	⋯	3582457858255051392	⋯	14.043 ± 0.040	
201050511	10	⋯	3582458579809568256	⋯	11.405 ± 0.030	
201051317	10	98321820422274493	3582459163925111552	⋯	15.285 ± 0.003	
201051625	10	⋯	3582459301364064768	⋯	12.821 ± 0.040	
201052484	10	⋯	3582465176879327488	⋯	13.713 ± 0.050	
201054099	10	98441820384293565	3582468612853166080	⋯	15.090 ± 0.003	
201054338	10	⋯	3582466619988381184	⋯	12.188 ± 0.050	
201054542	10	98461822154792184	3582466997945503616	⋯	14.871 ± 0.005	
201054991	10	98471821477879568	3582467582061055360	⋯	15.185 ± 0.003	
201071559	10	99101827692668111	3582605914368082816	⋯	16.649 ± 0.005	
201071583	10	99101826522918865	3582603406107179264	⋯	18.861 ± 0.014	
201071950	10	99121828753012622	3582605502051225216	⋯	14.848 ± 0.003	
201071997	10	99121826550054361	3582603440466918016	⋯	17.159 ± 0.004	
201072036	10	⋯	3594613577775506048	⋯	15.455 ± 0.020	
201072674	10	99141828915398845	3582607220038146176	⋯	14.921 ± 0.002	
201073202	10	⋯	3594613440336532224	⋯	15.761 ± 0.030	
201073315	10	99171829021981565	3582607323117362688	⋯	15.693 ± 0.060	
201073427	10	⋯	3594616154755833984	⋯	14.027 ± 0.020	
201073453	10	⋯	3594616253538685824	⋯	13.622 ± 0.040	
201073867	10	99191826959622285	3582610346774334336	⋯	17.607 ± 0.006	
201073911	10	99191829080563936	3582607421901033856	⋯	16.277 ± 0.006	
201074123	10	99201827274061451	3582610003176952320	⋯	17.683 ± 0.002	
201074212	10	⋯	3582609865738000000	⋯	11.700 ± 0.030	
201074534	10	99211822135945395	3594605709395368832	⋯	15.479 ± 0.004	
201074673	10	⋯	3594614608567639808	⋯	14.109 ± 0.020	
201074674	10	⋯	3594605812474584704	⋯	12.950 ± 0.030	
201074775	10	⋯	3582607834216399104	⋯	12.096 ± 0.030	
201074882	10	99221824760577057	3594618010181737088	⋯	14.993 ± 0.003	
201075355	10	99241827756634091	3582611652444397312	⋯	18.450 ± 0.007	
201075442	10	⋯	3594606774547212160	⋯	12.263 ± 0.030	

Note. There are 222,088 unique targets in this table. There were 19,829 targets observed in two or three campaigns, which we list as separate entries for each *K2* campaign. This table contains a total of 244,337 entries. Apparent *g*, *r*, and *i*-band magnitudes are from Pan-STARRS for targets with a Pan-STARRS ID and from UCAC4 or SDSS as reported in the EPIC (Huber et al. 2016) otherwise. Spectral type, $T_{\rm eff}$, log *g*, and [Fe/H] for stars with a LAMOST ID were derived using LAMOST spectra. These parameters for stars without a LAMOST ID were derived using photometry trained on the spectroscopic sample.

(This table is available in its entirety in machine-readable form.)

uses the University of Lyon Spectroscopic analysis Software spectrum fitting package (Koleva et al. 2009). For M dwarfs, spectral type and atomic and molecular line indices were determined using `The Hammer` (Covey et al. 2007), but other stellar parameters were not derived (Yi et al. 2014). We discuss derivation of stellar radii and masses for AFGK stars in Section 3. In Section 4, we compute $T_{\rm eff}$, log *g*, [Fe/H], $R_\star$, and $M_\star$ for M dwarfs.

3. AFGK Stellar Parameters

Since the LAMOST pipeline provides $T_{\rm eff}$, log *g*, and [Fe/H] for AFGK stars, we can readily compute stellar radii in a similar fashion to Fulton & Petigura (2018). We first computed bolometric magnitudes ($M_{\rm bol}$) from K_s-band measurements, since K_s is less affected by interstellar extinction than the other optical and near-infrared photometric bands:

$$M_{\rm bol} = m_{K_s} - 5[\log_{10}(d) - 1] - A_{K_s} - BC, \quad (2)$$

where *d* is the distance computed from *Gaia* parallax measurements (Bailer-Jones et al. 2018), A_{K_s} is the K_s-band interstellar extinction computed using `dustmaps` (Green et al. 2018), and BC is the bolometric correction. Bolometric corrections were computed using `isoclassify`, which interpolates the Modules for Experiments in Stellar Astrophysics Isochrones and Stellar Tracks grid (Dotter 2016) over $T_{\rm eff}$, log *g*, [Fe/H], and A_{K_s}. Bolometric luminosity ($L_{\rm bol}$) was calculated from bolometric magnitudes using:

$$L_{\rm bol} = L_0 10^{-0.4 M_{\rm bol}}, \quad (3)$$

where $L_0 \equiv 3.0128 \times 10^{28}$ W (Mamajek et al. 2015). Finally, we computed $R_\star$ from the Stefan–Boltzmann law:

$$R_\star = \left(\frac{L_{\rm bol}}{4\pi\sigma_{\rm SB} T_{\rm eff}^4} \right)^{1/2}, \quad (4)$$

where $\sigma_{\rm SB}$ is the Stefan–Boltzmann constant. Since we have both $R_\star$ and log *g* measurements, $M_\star$ was computed using $M_\star = 10^{\log g} \times R_\star^2 / G$, where *G* is the gravitational constant.

Uncertainties for parameters in this paper were computed using a Monte Carlo approach. For targets with symmetric

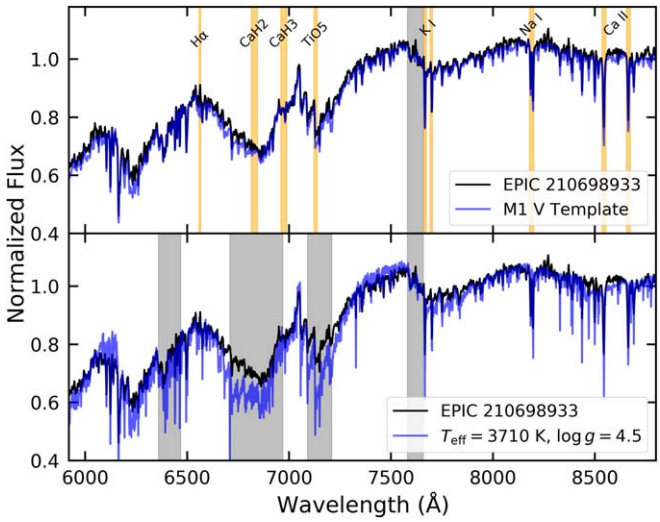

Figure 4. Top: LAMOST spectrum of EPIC 210698933 (black) compared to an M1 *V* spectral template from Kesseli et al. (2017) (blue). A few prominent M dwarf atomic lines and molecular indices are indicated by the orange regions. Bottom: the same spectrum compared to the closest matching PHOENIX-ACES model. Regions where the templates or models poorly matched the LAMOST spectra were masked out in the fitting process, which we show here in gray.

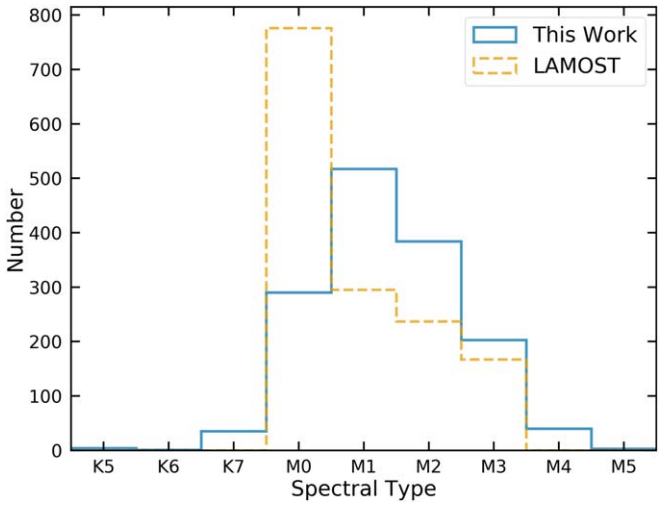

Figure 5. Comparison of spectral type classifications between LAMOST (dashed) and our pipeline (solid).

uncertainties, we drew 10^4 samples from a Gaussian distribution for each measured value and associated uncertainty. For targets with asymmetric uncertainties, we drew 10^4 samples from a split normal distribution, combining the left and right sides of two Gaussian distributions centered on the measured value and the negative and positive uncertainties. We propagated these distributions through each equation and took the median of the resultant distribution as the measured value and the 15.87 and 84.13 percentiles as the uncertainties. The average uncertainties on $R_\star$ and $M_\star$ for AFGK stars with LAMOST spectra are 4.4% and 14.9%, respectively. The very low uncertainties on these measurements are due to the $\sim$1% uncertainties on $T_{\rm eff}$ and log g provided by the LAMOST pipeline for high-S/N targets.

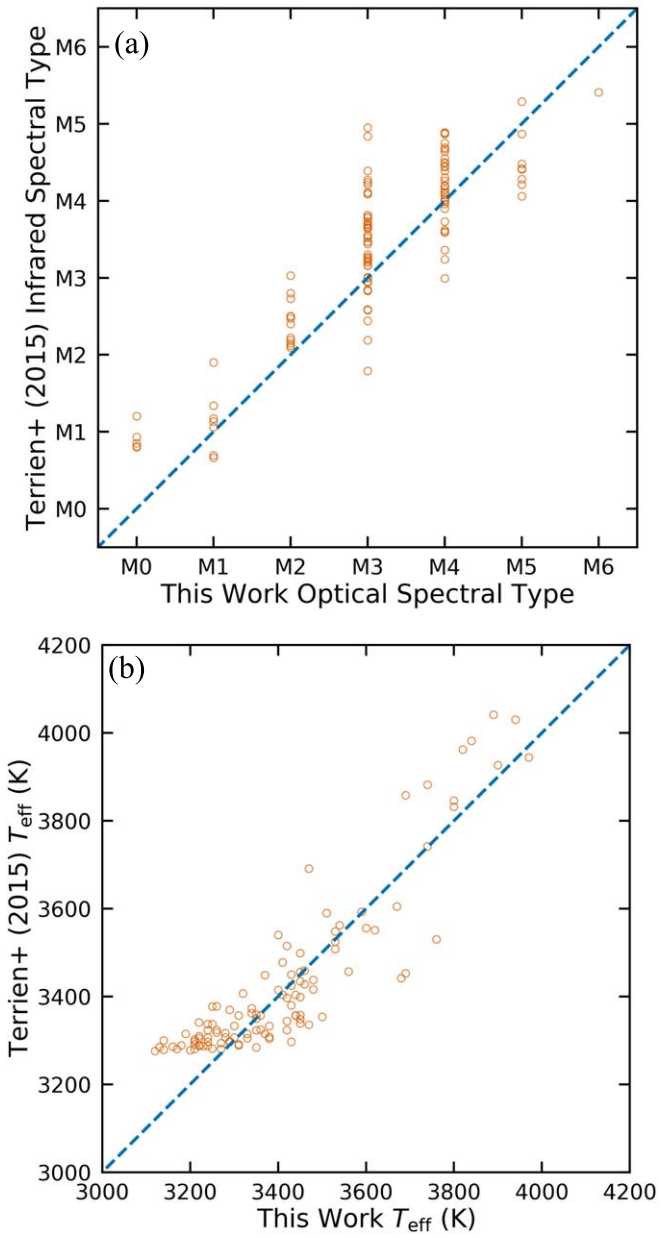

Figure 6. (a) Comparison of infrared spectral types from Terrien et al. (2015) to our optical spectral types from LAMOST spectra. The optical spectral types are on average half a spectral type earlier than those from infrared spectra. (b) Effective temperatures from infrared and optical spectra are similar, but the infrared spectra temperature relationships used in Terrien et al. (2015) are only valid down to a range of 3300 K, which explains the sharp cut-off in the plot.

4. M Dwarf Parameters

4.1. Spectral Type

The LAMOST data do not include $T_{\rm eff}$, log g, and [Fe/H] for M dwarfs, so we derived our own parameters for these stars. M dwarfs in the LAMOST catalog were initially classified using a modified version of `The Hammer` (Covey et al. 2007), then they were visually inspected, which changed the classification of nearly one-fifth of the stars (Yi et al. 2014). Since visual inspection can introduce bias, we reran the spectral typing of our LAMOST M dwarfs in a uniform automated process using the spectral templates of Kesseli et al. (2017). These templates were derived from thousands of SDSS Baryon Oscillation Spectroscopic Survey spectra, covering 3600–10,400 Å at a

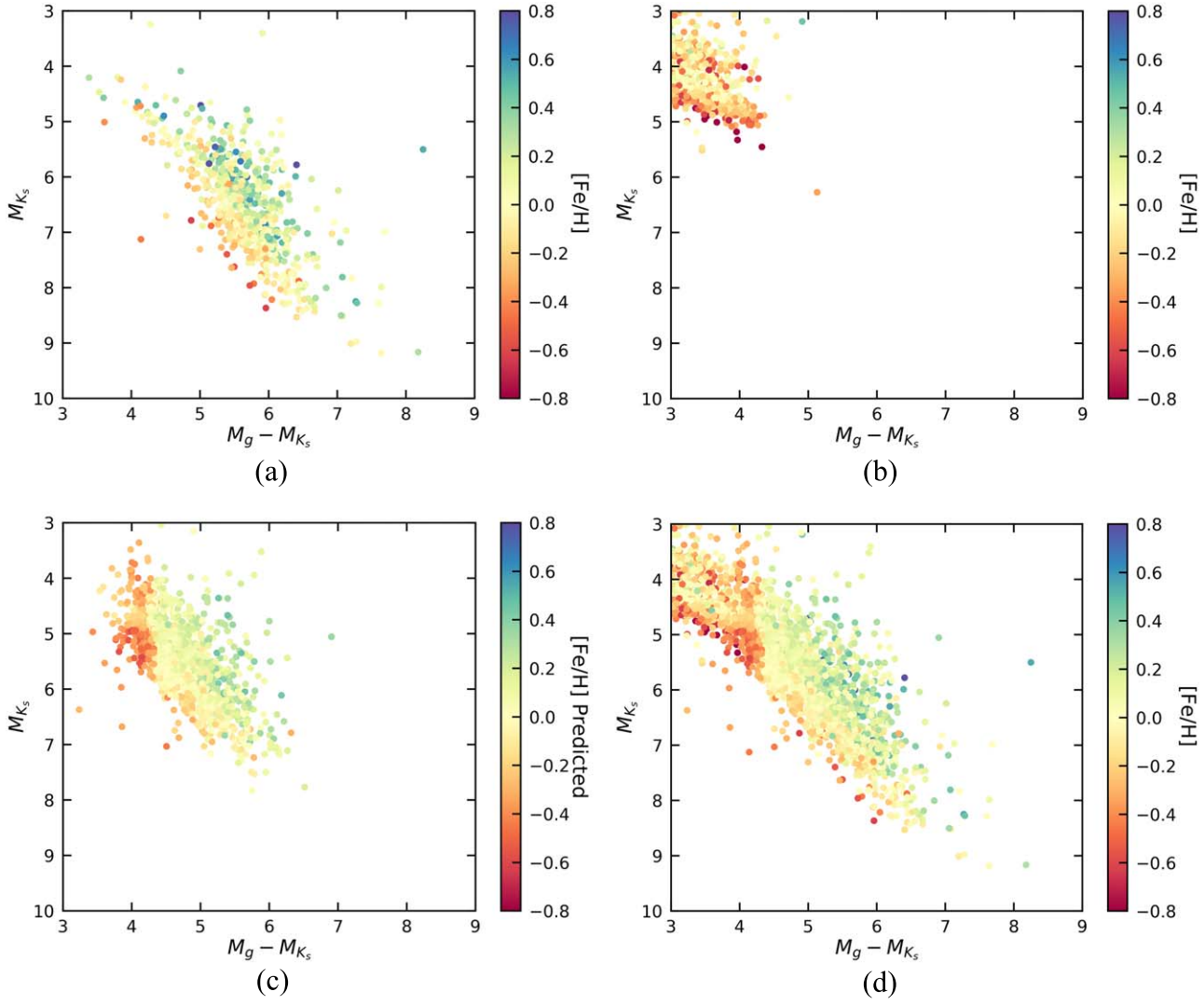

Figure 7. Color–magnitude diagrams colored by [Fe/H] for the Terrien et al. (2015) M dwarf sample (a) and our LAMOST FGK targets (b). The results for the LAMOST M dwarf [Fe/H] classification are shown in (c), and these results are combined with (a) and (b) in panel (d).

resolution of $R \approx 2000$ (Dawson et al. 2013). We used the K5 to M7 dwarf templates, which are separated into 0.5 dex metallicity bins. We resampled the template spectra to match the resolution of the LAMOST spectra using `SpectRes`[14] (Carnall 2017). To identify the closest matching spectral template, we minimize the goodness-of-fit statistic G_K (Equation 1 of Cushing et al. 2008), which is similar to χ^2 minimization. In order to identify regions where the templates poorly fit our spectra, we ran the spectrum matching twice. First, using the same methods described in Section 5.1 of Mann et al. (2013b), we computed the residuals from the best-fit spectral template for each of the LAMOST spectra, then computed the median fractional deviation between the data and the templates at each wavelength. Regions with a median deviation greater than 10% were given a weight of 0 in G_K for the second round of spectrum matching. This applied to $\lambda < 5910$ Å, 7580 Å $< \lambda <$ 7660 Å, and $\lambda >$ 8800 Å. The poor fit at blue wavelengths might be due to the nature of the LAMOST spectra, which are taken in two different channels (3700–5900 Å and 5700–9000 Å; Cui et al. 2012) and combined during processing. Spectral typing of M dwarfs has historically been done at red wavelengths (e.g., Kirkpatrick et al. 1991), so we made no additional attempt to fit the red and blue regions separately. In the top panel of Figure 4 we show an example M-dwarf spectrum compared to its closest matching spectral template, with prominent atomic lines (Hα, K I, Na I, and Ca II) and molecular indices (CaH2, CaH3, and TiO5) identified. In Figure 5, we compare our spectral types to those from the LAMOST pipeline for the same targets. Our classifications are more evenly distributed among the early M types with a peak near M1, whereas the LAMOST spectral types are significantly skewed toward M0. About 97% of our targets are within one spectral type of the LAMOST classification. We also identified a few late K-dwarf interlopers that were assigned an M spectral type by LAMOST. We derived parameters for these K dwarfs in the same manner as our spectroscopic M dwarfs described below.

4.2. Effective Temperatures

We compared the LAMOST spectra to the PHOENIX–ACES model grid from Husser et al. (2013), which were sampled in increments of $T_{\rm eff} = 100$ K, log $g = 0.5$, and

[14] https://github.com/ACCarnall/spectres

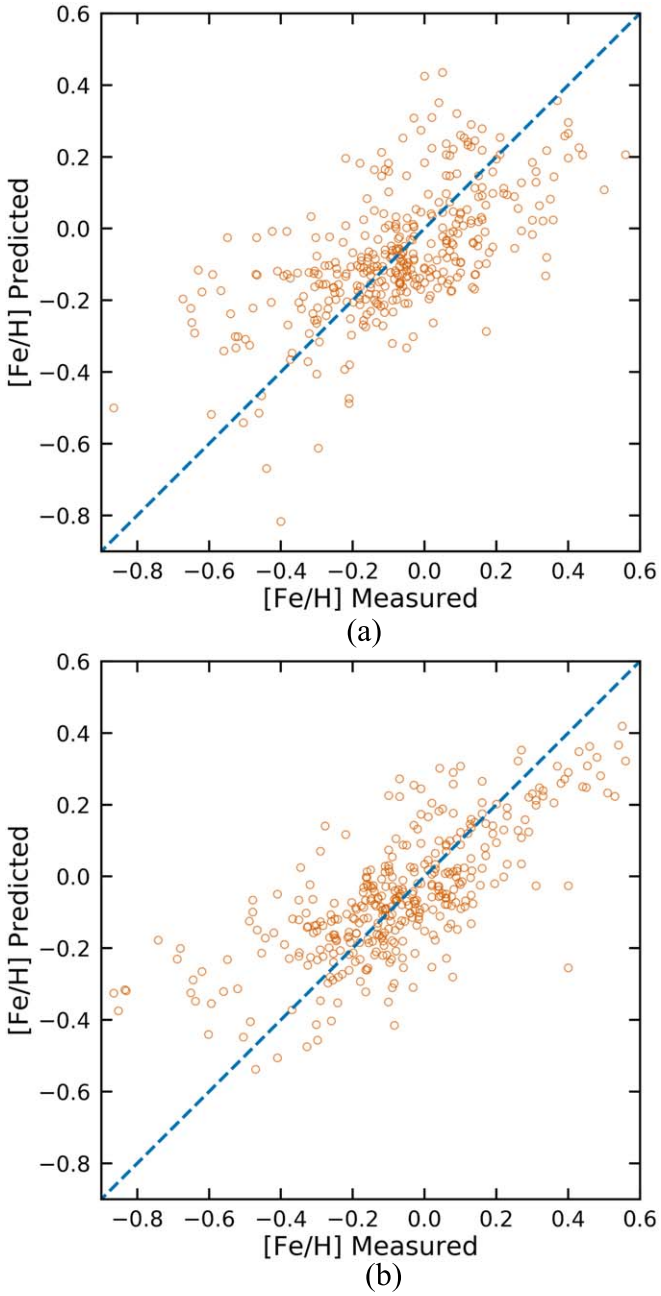

Figure 8. (a) Comparison of predicted vs. measured [Fe/H] from our random forest regression using only M_{K_s} and $M_g - M_{K_s}$ and (b) using $M_g - M_r$, $M_r - M_i$, $M_i - M_J$, $M_J - M_H$, and $M_H - M_{K_s}$, which yields a tighter correlation. The 1:1 lines are plotted for reference.

[Fe/H] = 0.5. From these model spectra, we interpolated a finer model grid to $T_{\rm eff} = 10$ K and log $g = 0.1$, using [Fe/H] = 0 models. To identify the closest matching model spectrum, we used the same procedure outlined in Section 4.1, this time masking out the following regions: $\lambda < 5920$ Å, 6360 Å $< \lambda <$ 6470 Å, 6710 Å $< \lambda <$ 6970 Å, 7090 Å $< \lambda <$ 7210 Å, 7580 Å $< \lambda <$ 7660 Å, and $\lambda > 8800$ Å. In the bottom panel of Figure 4, we show the example spectrum compared to its closest matching spectral model, indicating regions that were masked out due to poor model fits. We adopt the temperatures from the closest matching spectral model, but we refine our surface gravity measurements in Section 4.4.

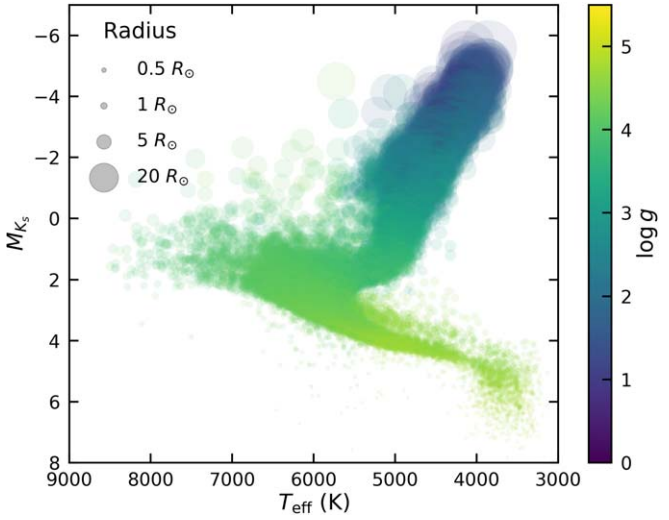

Figure 9. HR diagram LAMOST targets. Colors indicate surface gravity, and the size of the points represent stellar radius.

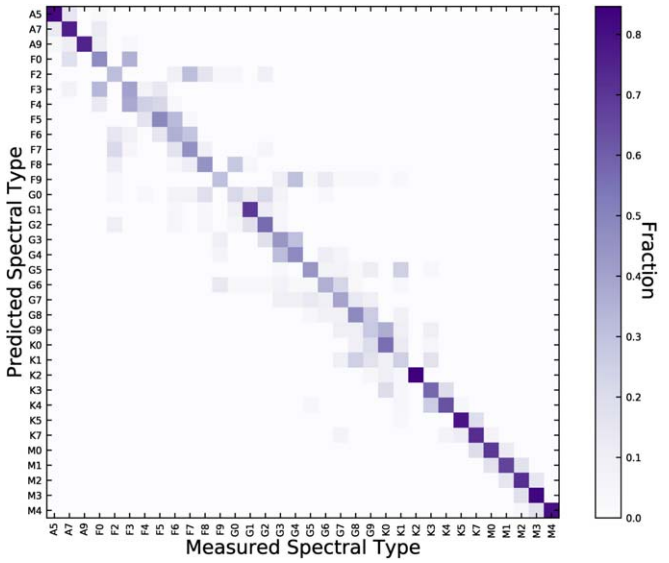

Figure 10. Measured vs. predicted spectral types from our random forest classification, showing a reasonable prediction for most targets.

Table 2
Number of Targets in Our LAMOST Sample with Each Spectral Type Classification

Type	#	Type	#	Type	#	Type	#
A1	6	F3	179	G3	2399	K3	682
A2	2	F4	131	G4	580	K4	280
A3	7	F5	1649	G5	4009	K5	457
A5	23	F6	639	G6	669	K7	245
A6	33	F7	1038	G7	1762	M0	278
A7	109	F8	276	G8	1266	M1	496
A8	10	F9	2122	G9	563	M2	377
A9	13	G0	915	K0	363	M3	195
F0	962	G1	328	K1	1155	M4	40
F2	703	G2	1861	K2	17	M5	2

Terrien et al. (2015) conducted a near-infrared spectroscopic survey of 886 nearby M dwarfs, from which they identified spectral types and measured temperatures and metallicities. From this list, we found a matching LAMOST spectrum for

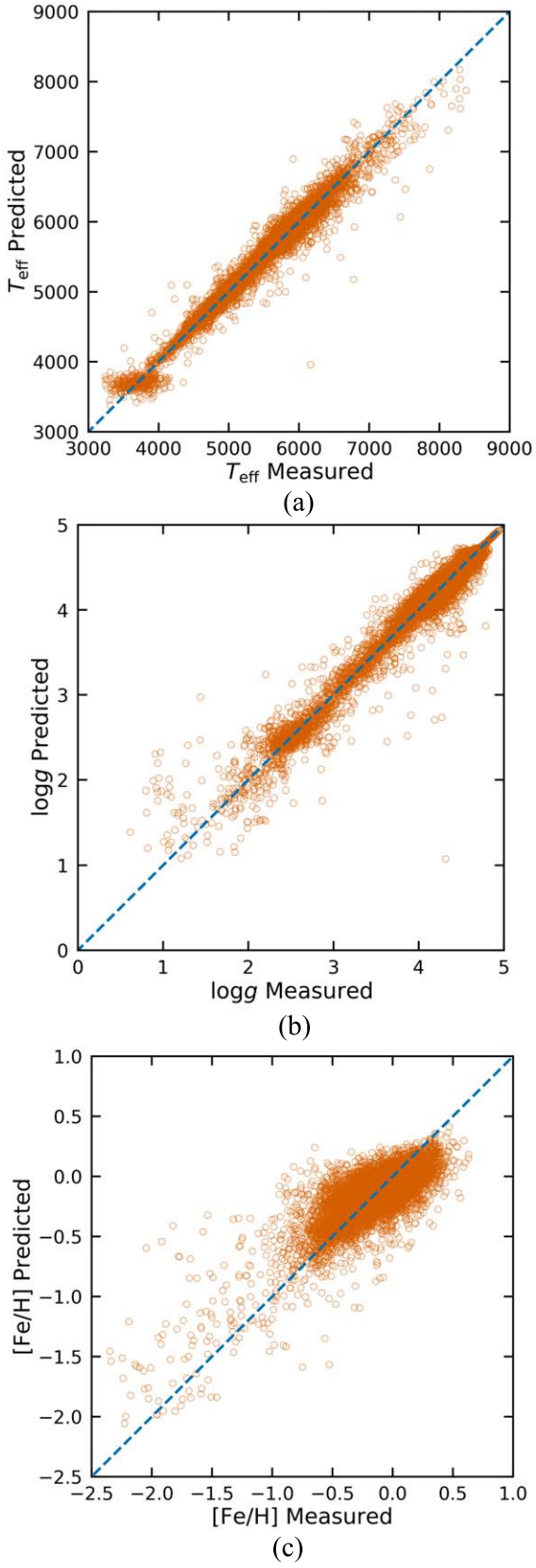

Figure 11. Comparison of predicted vs. measured $T_{\rm eff}$ (a), log g (b), and [Fe/H] (c) from our random forest regression using M_{K_s}, $M_g - M_{K_s}$, $M_g - M_r$, $M_r - M_i$, $M_i - M_J$, $M_J - M_H$, and $M_H - M_{K_s}$. The 1:1 lines are plotted for reference. There are tight correlations for $T_{\rm eff}$ and log g, as well as a positive correlation for [Fe/H].

108 targets that match our criteria above, which allows us to compare results from our methods. Terrien et al. (2015) identified spectral types using a spectroscopic H_2O–K2 index typing method first used by Rojas-Ayala et al. (2012) and updated by Newton et al. (2014). Our spectral types are on average a spectral type earlier than Terrien et al. (2015), which is illustrated in Figure 6(a). For consistency with the spectral typing of earlier-type stars, we recommend using spectral types based on optical spectra rather than infrared spectra when possible. Effective temperatures in Terrien et al. (2015) were measured using K_s-band index calibrations from Mann et al. (2013b), which are valid in the range 3300 K $< T_{\rm eff} <$ 4800 K. We compared our derived temperatures in Figure 6(b), which shows the sharp temperature cutoff in the Terrien et al. (2015) data at 3300 K. Our temperatures are on average 20 K less than those of Terrien et al. (2015). Due to the similarity between temperature scales, we adopt the rms scatter of 93 K for our $T_{\rm eff}$ uncertainties.

4.3. Metallicity

The myriad molecular lines at optical wavelengths hinder the measurement of metallicity from moderate resolution optical spectra. Metallicity for M dwarfs can be directly measured if they have a wide-separation F, G, or K-dwarf primary companion, assuming the stars formed at the same time from the same molecular cloud (Bonfils et al. 2005). These stars allow the calibration of absolute photometric (e.g., Bonfils et al. 2005; Johnson & Apps 2009; Schlaufman & Laughlin 2010; Neves et al. 2012) and moderate-resolution spectroscopic (e.g., Rojas-Ayala et al. 2010, 2012; Terrien et al. 2012; Mann et al. 2013a, 2014; Newton et al. 2014) methods. From moderate-resolution optical spectra, the ζ parameter, computed from TiO and CaH spectroscopic indices, has shown a weak correlation with metallicity (e.g., Woolf et al. 2009; Mann et al. 2013a), and the LAMOST pipeline provides measurements of ζ for M dwarfs. Mann et al. (2013a) compared different methods for computing M-dwarf metallicities, and found that the highest quality calibrations come from K-band features from moderate resolution infrared spectra.

We initially tried to use the spectral indices and ζ measurements provided by the LAMOST pipeline to determine metallicity on the set of 108 stars with both a LAMOST spectrum and a K-band metallicity measurement from Terrien et al. (2015), but we could not find any strong correlations. Instead, we calibrated a photometric metallicity relationship using 636 M dwarfs from Terrien et al. (2015) that have metallicity measurements, *Gaia* parallaxes, and g, r, i, J, H, and K_s-band photometry. We first computed absolute magnitudes for these targets. In Figure 7(a), we plot M_{K_s} versus $M_g - M_{K_s}$, with color indicating measured [Fe/H]. In this color space, there appears to be a metallicity gradient for M dwarfs, with larger $M_g - M_{K_s}$ colors generally indicating higher metallicity for the same M_{K_s} magnitude. Due to the paucity of Terrien et al. (2015) targets with $M_g - M_{K_s} < 5$, we also included 1483 of our LAMOST AFGK targets with measured metallicities, $M_{K_s} > 3$, and $M_g - M_{K_s} > 3$ (Figure 7(b)). We trained a random forest regressor (`scikit-learn`; Pedregosa et al. 2011) with 1000 trees on M_{K_s} and $M_g - M_{K_s}$ for a random subset of 75% of the 2,119 targets with measured metallicities. We used the remaining 25% of targets to determine how well the regressor

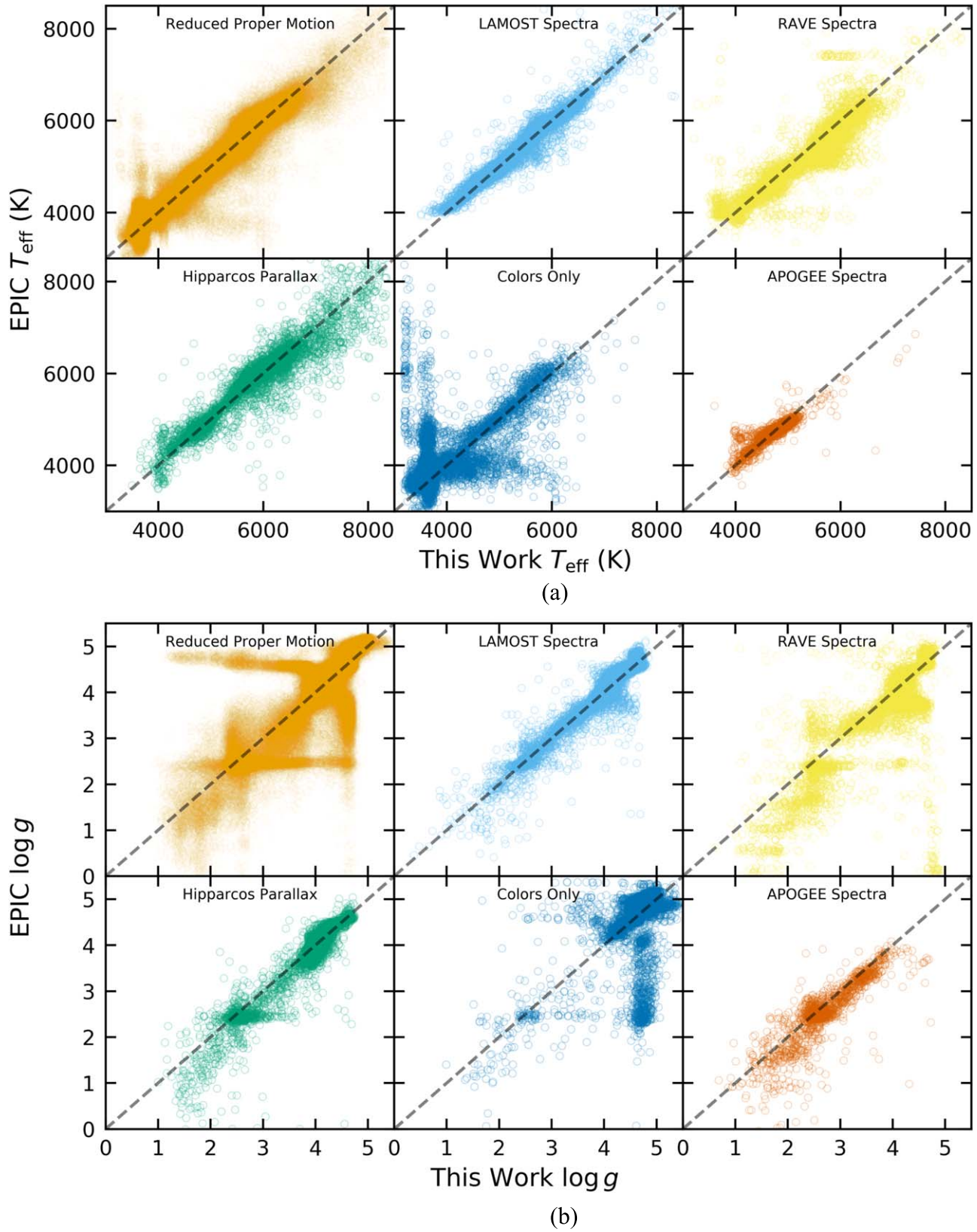

Figure 12. Comparison of our temperature (a) and surface gravity (b) measurements to those from the EPIC. Each panel compares our measurements to the different methods used to derive the parameters in the EPIC, which allows us to elucidate any potential trends based on classification method.

performed. Figure 8(a) compares the measured [Fe/H] to the predicted [Fe/H] from the random forest regressor. The median rms scatter from 1000 different random forest regressions using only M_{K_s} and $M_g - M_{K_s}$ is 0.19. When we also included $M_g - M_r$, $M_r - M_i$, $M_i - M_J$, $M_J - M_H$, and $M_H - M_{K_s}$ as input parameters in the random forest

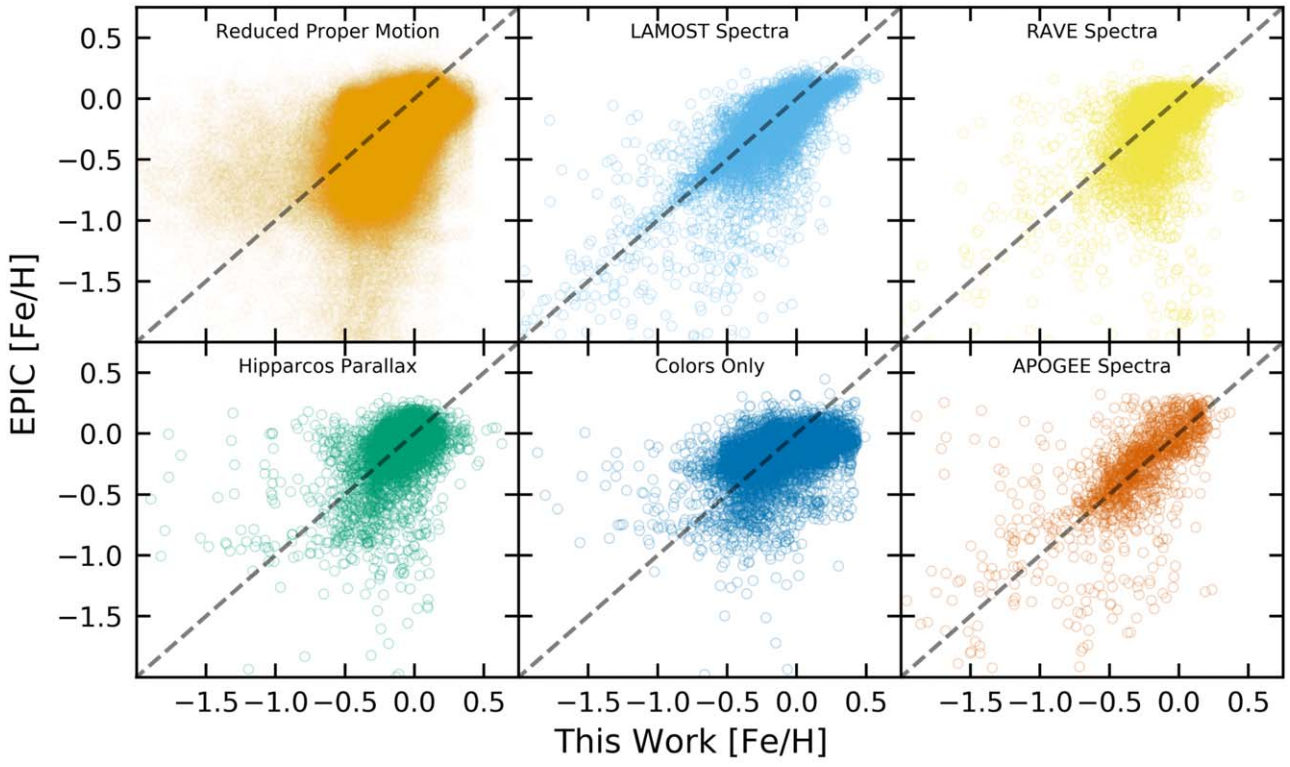

Figure 13. Same as Figure 12, but for metallicity (a) and stellar radii (b).

regression, the median rms scatter reduced to 0.17 (Figure 8(b)), which we took as the uncertainty in our M star [Fe/H] measurements. We plot the results from the [Fe/H] regression in Figures 7(c) and (d).

4.4. Radius, Mass, and Surface Gravity

Mann et al. (2015) and Mann et al. (2019) derived empirical M_{K_s}–$R_\star$ and M_{K_s}–$M_\star$ relationships for M dwarfs to a precision below 3%. We used these relationships to compute radii and

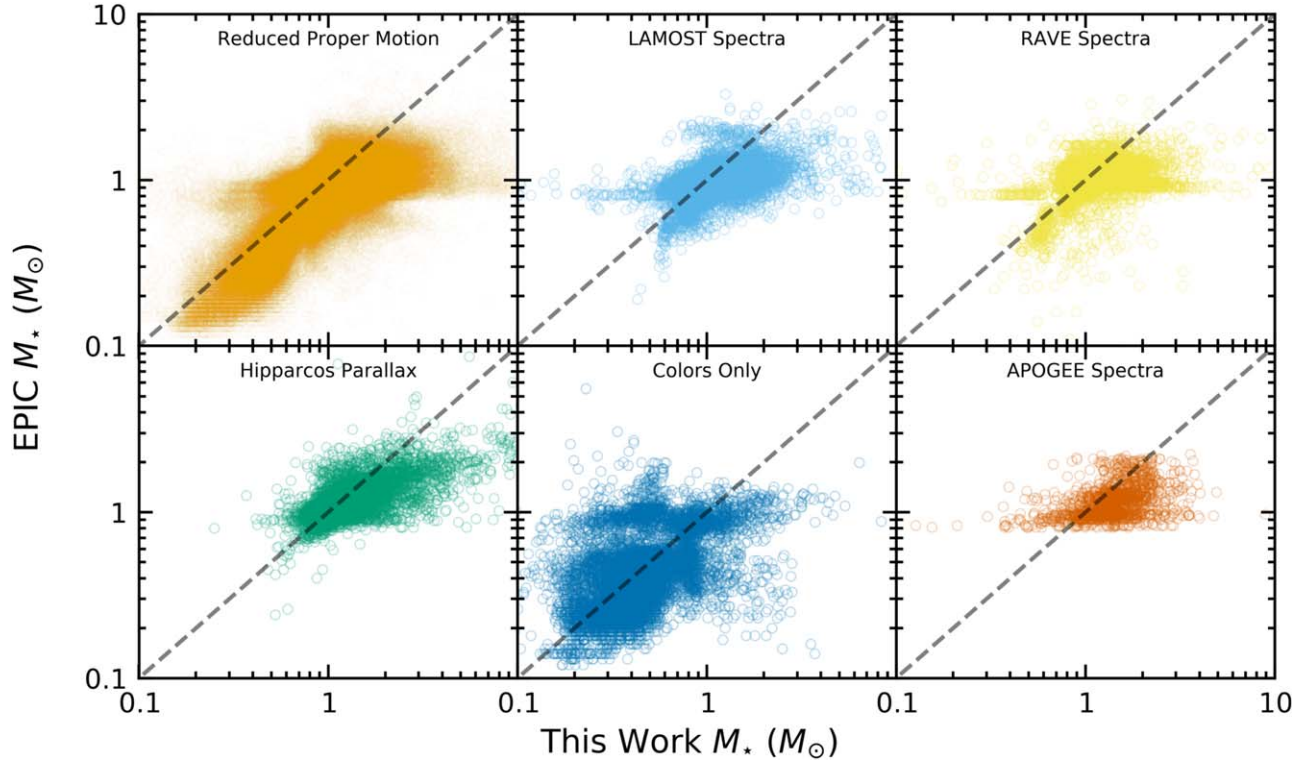

Figure 14. Same as Figure 12, but for stellar mass.

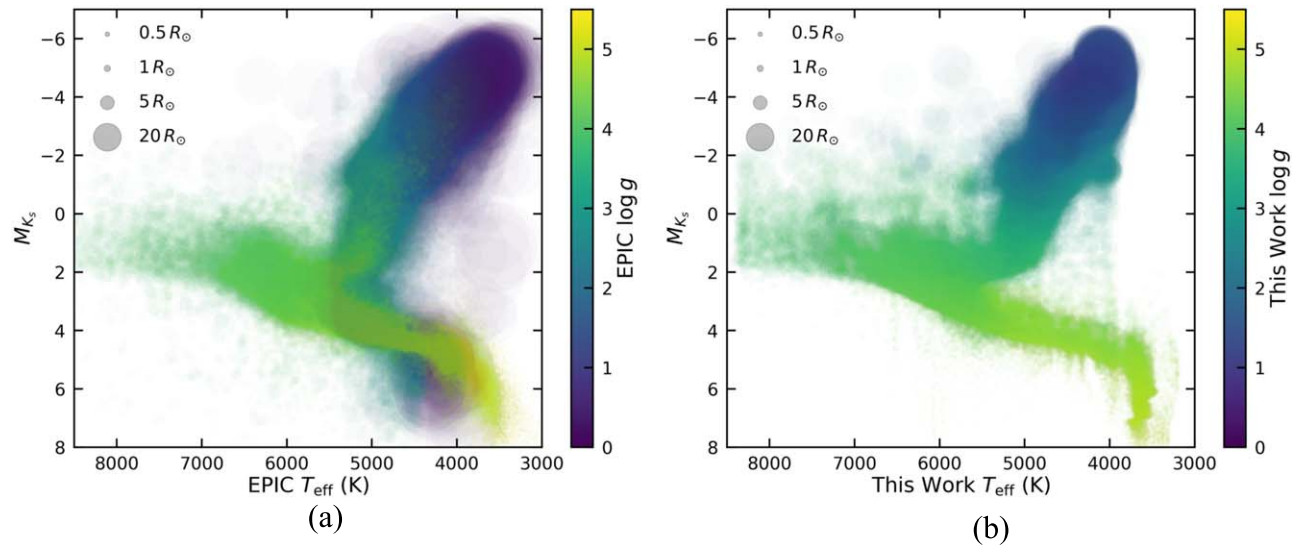

Figure 15. HR diagrams for (a) EPIC parameters and (b) our parameters. Colors indicate surface gravity, and the size of the points represent stellar radius. Several giant-dwarf interlopers are clearly visible in the EPIC HR diagram.

masses of our M dwarfs. We added the model uncertainties from Mann et al. (2015) and Mann et al. (2019) in quadrature to our calculated Monte Carlo uncertainties, yielding average radius and mass uncertainties of 3.1% and 6.6%, respectively. From mass and radius, we calculated surface gravity for these stars using $\log g = \log(GM_\star/R_\star^2)$. We list all spectroscopically derived stellar parameters for AFGK and M stars in Table 1 and show a Hertzsprung–Russell (HR) diagram of all LAMOST targets in Figure 9.

5. Photometric Classification

Using the 26,838 *K2* targets classified from LAMOST spectra and *Gaia* parallaxes, we then classified stars with only photometry and *Gaia* parallaxes. The first step was to compute absolute magnitudes and the following colors to use for classification: $M_g - M_{K_s}$, $M_g - M_r$, $M_r - M_i$, $M_i - M_J$, $M_J - M_H$, and $M_H - M_{K_s}$. We first restricted our sample to *K2* stars with these colors within the range of the LAMOST targets. This is necessary because random forest classification

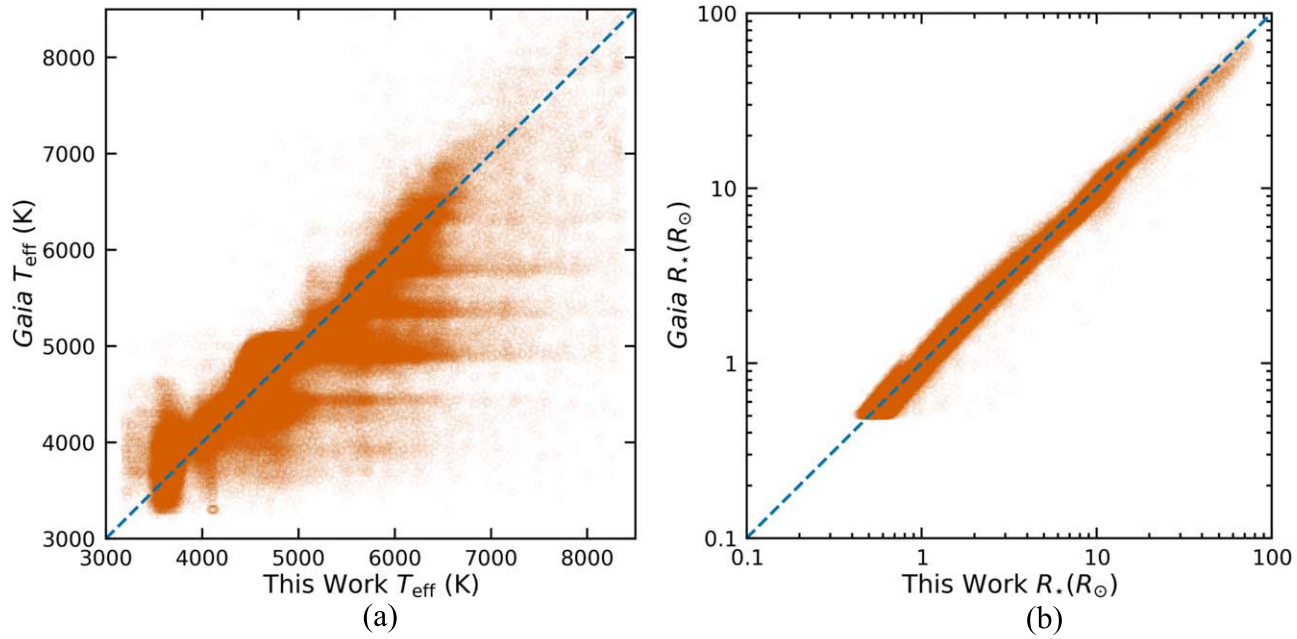

Figure 16. Comparison of our temperature (a) and stellar radius (b) measurements to those from *Gaia*. We caution readers to be careful when using *Gaia* effective temperatures. It is also noteworthy that *Gaia* does not contain radius measurements for most M dwarfs smaller than 0.5 $R_\odot$.

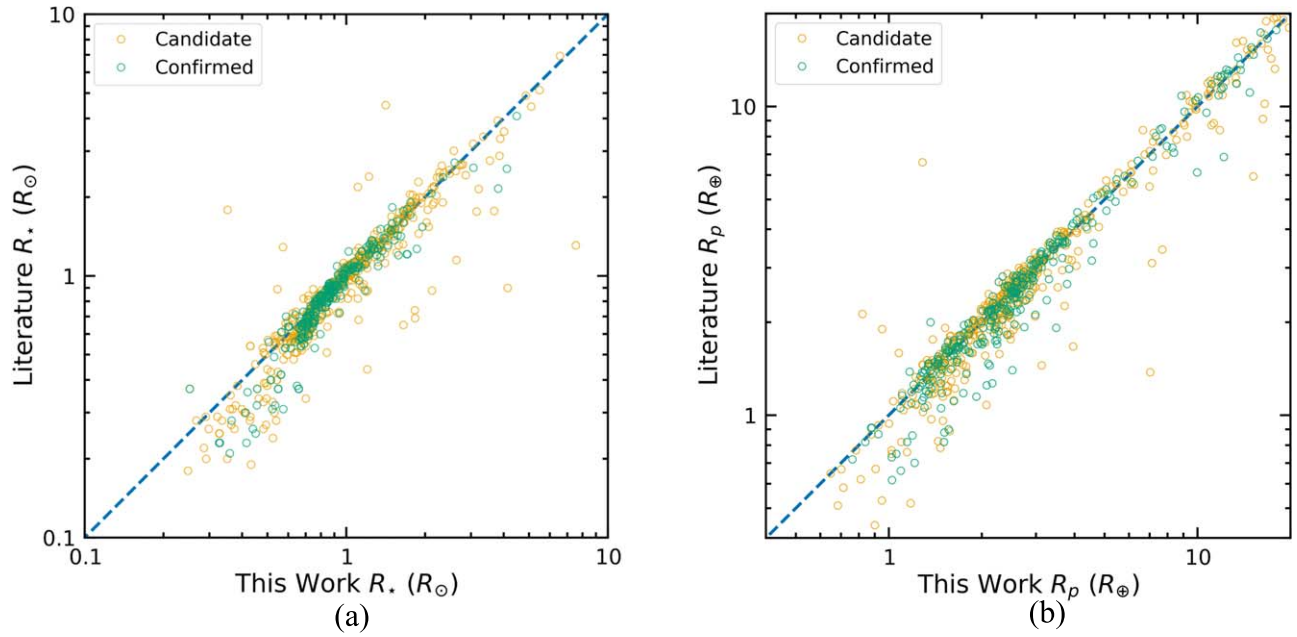

Figure 17. Comparison of literature stellar radii (a) and planet radii (b) vs. our measurements for confirmed and candidate hosts. Our radii for stars smaller than the Sun are typically larger than the values in the literature.

and regression cannot extrapolate beyond the range of the training set. This removed 9673 targets from our sample, leaving us with 195,250 non-spectroscopic targets, and a total sample of 222,088 targets. A majority of the targets that were removed are fainter than $Kp = 18$ (Figure 1).

We began classification with spectral types. Table 2 shows the number of targets with each spectral type in our LAMOST sample. Due to the relatively small numbers of A-type stars, we grouped A1–A6 stars into A5, and A8–A9 into A9 to increase the numbers in each respective bin for classification. In order to minimize bias due to different sample sizes, we randomly selected 100 stars from each spectral type to use for classification. For A5, A9, K2, and M4, we randomly sampled with replacement. In a similar manner to Section 4.3, we used these aforementioned colors along with M_{K_s} to train a random forest classifier (`scikit-learn`; Pedregosa et al. 2011) with 1000 trees on a random subset of 75% of the spectroscopic target subsample. The remaining 25% of the subsample were used to check the classifier performance. Figure 10 shows the measured versus predicted spectral type from the testing set. A majority of the predicted classifications are along or near the diagonal, indicating the classifier does a reasonable job at predicting spectral type. We used the trained classifier on all the photometric targets to yield spectral types. The assigned spectral types from photometry should be adequate for large statistical studies of *K2* targets, but we caution their use for

Table 3
Refined *K2* Planet Parameters

EPIC ID	Candidate ID	Confirmed Planet Name	$R_p/R_\star$	Period (days)	Reference	Spectral Type	⋯
201110617	201110617.01	K2-156 b	$0.01704^{+0.00139}_{-0.00114}$	$0.813149^{+0.000050}_{-0.000049}$	5	K5	
201111557	201111557.01	⋯	$0.01692^{+0.00674}_{-0.00148}$	$2.302368^{+0.000105}_{-0.000103}$	5	K3	
201127519	201127519.01	⋯	$0.11511^{+0.00492}_{-0.00336}$	$6.178369^{+0.000195}_{-0.000172}$	5	K3	
201130233	201130233.01	K2-157 b	$0.01105^{+0.00143}_{-0.00097}$	$0.365257^{+0.000029}_{-0.000029}$	5	G7	
201132684	201132684.01	K2-158 b	$0.02707^{+0.00275}_{-0.00198}$	$10.062106^{+0.00227}_{-0.002228}$	5	G7	
201152065	201152065.01	⋯	$0.0226^{+0.0022}_{-0.0055}$	$10.6966^{+0.002}_{-0.0021}$	3	K5	
201155177	201155177.01	K2-42 b	$0.0313^{+0.0023}_{-0.0047}$	$6.68851^{+0.00074}_{-0.00075}$	3	K5	
201160662	201160662.01	⋯	$0.259^{+0.071}_{-0.099}$	$1.5374115^{+0.0000062}_{-0.0000061}$	3	F6	
201166680	201166680.01	⋯	$0.01572^{+0.00173}_{-0.00119}$	$18.10549^{+0.010083}_{-0.012897}$	5	F2	
201176672	201176672.01	⋯	$0.18^{+0.011}_{-0.011}$	$79.9999^{+0.0098}_{-0.0098}$	2	K5	
201197348	201197348.01	⋯	$0.046^{+0.0038}_{-0.0078}$	$14.9139^{+0.0018}_{-0.002}$	3	K5	
201205469	201205469.01	K2-43 b	$0.0775^{+0.0034}_{-0.0063}$	$3.471136^{+0.000079}_{-0.000079}$	3	M1	
201205469	201205469.02	K2-43 c	$0.0391^{+0.0039}_{-0.0113}$	$2.19945^{+0.00015}_{-0.00014}$	3	M1	
201208431	201208431.01	K2-4 b	$0.0368^{+0.0015}_{-0.0031}$	$10.0051^{+0.00044}_{-0.00043}$	3	K7	
201211526	201211526.01	K2-244 b	$0.01698^{+0.00312}_{-0.00127}$	$21.070201^{+0.002413}_{-0.002267}$	5	G3	
201225286	201225286.01	K2-159 b	$0.02439^{+0.00226}_{-0.00134}$	$12.421078^{+0.001049}_{-0.001001}$	5	G7	
201227197	201227197.01	K2-160 b	$0.03189^{+0.00171}_{-0.00114}$	$3.705871^{+0.000074}_{-0.000076}$	5	G4	
201231064	201231064.01	K2-161 b	$0.02184^{+0.00518}_{-0.00181}$	$9.283188^{+0.002052}_{-0.0023}$	5	G5	
201238110	201238110.01	⋯	$0.0505^{+0.005}_{-0.0129}$	$7.90417^{+0.00091}_{-0.00148}$	3	M2	
201238110	201238110.02	EPIC 201238110 b	$0.054^{+0.0034}_{-0.0054}$	$28.1696^{+0.0038}_{-0.0043}$	3	M2	
201239401	201239401.01	⋯	$0.025^{+0.0019}_{-0.0039}$	$0.905655^{+0.000049}_{-0.000050}$	3	M2	
201247497	201247497.01	⋯	$0.087^{+0.011}_{-0.07}$	$2.75421^{+0.00012}_{-0.00012}$	3	M0	
201259803	201259803.01	⋯	$0.1173^{+0.0034}_{-0.0035}$	$1.684208^{+0.000024}_{-0.000024}$	3	M1	
201264302	201264302.01	⋯	$0.0253^{+0.0018}_{-0.006}$	$0.2122013^{+0.0000023}_{-0.0000018}$	3	M3	
201295312	201295312.01	K2-44 b	$0.01775^{+0.00066}_{-0.00165}$	$5.65621^{+0.00026}_{-0.00027}$	3	G0	
201299088	201299088.01	⋯	$0.04741^{+0.00197}_{-0.00184}$	$21.204739^{+0.005348}_{-0.005523}$	5	G8	
201324549	201324549.01	⋯	$0.089^{+0.022}_{-0.039}$	$2.519386^{+0.000014}_{-0.000014}$	3	F5	
201338508	201338508.01	K2-5 c	$0.0348^{+0.0031}_{-0.0079}$	$10.93459^{+0.00088}_{-0.00105}$	3	K7	
201338508	201338508.02	K2-5 b	$0.073^{+0.021}_{-0.039}$	$5.73649^{+0.00033}_{-0.00034}$	3	K7	
201345483	201345483.01	K2-45 b	$0.1431^{+0.005}_{-0.0044}$	$1.7292577^{+0.0000049}_{-0.0000050}$	3	K5	
201352100	201352100.01	⋯	$0.03231^{+0.00186}_{-0.00145}$	$13.383629^{+0.00076}_{-0.000727}$	5	K1	
201357835	201357835.01	⋯	$0.03044^{+0.001}_{-0.00079}$	$11.8951^{+0.0014}_{-0.0017}$	7	F8	
201359834	201359834.01	⋯	$0.266^{+0.081}_{-0.128}$	$40.1401^{+0.0012}_{-0.0012}$	3	M1	
201366540	201366540.01	⋯	$0.0346^{+0.0054}_{-0.0295}$	$7.4433^{+0.0011}_{-0.0012}$	3	K7	
201367065	201367065.01	K2-3 b	$0.0358^{+0.0012}_{-0.0031}$	$10.05467^{+0.00011}_{-0.00011}$	3	M1	
201367065	201367065.02	K2-3 c	$0.0291^{+0.0027}_{-0.0027}$	$24.64671^{+0.00054}_{-0.00053}$	3	M1	
201367065	201367065.03	K2-3 d	$0.0273^{+0.0029}_{-0.0048}$	$44.5574^{+0.0023}_{-0.0023}$	3	M1	
201384232	201384232.01	K2-6 b	$0.0259^{+0.0013}_{-0.003}$	$30.9403^{+0.0023}_{-0.0027}$	3	G3	
201390048	201390048.01	K2-162 b	$0.01878^{+0.00206}_{-0.00141}$	$9.457747^{+0.001401}_{-0.001392}$	5	K5	
201393098	201393098.01	K2-7 b	$0.0247^{+0.0015}_{-0.0036}$	$28.6911^{+0.0037}_{-0.0042}$	3	G6	
201403446	201403446.01	K2-46 b	$0.01764^{+0.00086}_{-0.0021}$	$19.153^{+0.002}_{-0.0022}$	3	F6	
201427874	201427874.01	K2-163 b	$0.02966^{+0.00301}_{-0.0014}$	$6.673117^{+0.000316}_{-0.000303}$	5	K4	
201437844	201437844.01	HD 106315 b	$0.01677^{+0.00101}_{-0.00067}$	$9.554515^{+0.001256}_{-0.001368}$	5	F4	

References. (1) Adams et al. (2016); (2) Crossfield et al. (2016); (3) Kruse et al. (2019); (4) Mann et al. (2017); (5) Mayo et al. (2018); (6) Osborn et al. (2016); (7) Zink et al. (2019).

(This table is available in its entirety in machine-readable form.)

individual targets and strongly encourage obtaining a spectrum for accurate spectral typing.

For effective temperature, surface gravity, and metallicity, we followed the same procedure outlined in Section 4.3, training a random forest regressor on M_{K_s}, $M_g - M_{K_s}$, $M_g - M_r$, $M_r - M_i$, $M_i - M_J$, $M_J - M_H$, and $M_H - M_{K_s}$ for our targets with spectroscopic $T_{\rm eff}$, log g, and [Fe/H] measurements. Figure 11 shows the results from the testing set, with good fits for $T_{\rm eff}$ and log g, and a positive correlation for [Fe/H]. We adopted the rms scatter as the uncertainties for photometrically classified targets, which are 138 K, 0.15 dex, and 0.20 dex for $T_{\rm eff}$, log g, and [Fe/H], respectively. Stellar radii and masses were then computed using the same procedures outlined in Section 3 for AFGK stars, and Section 4.4 for M stars. Average uncertainties on $R_\star$ and $M_\star$ for photometrically classified targets are 7% and 38%, respectively. We list the parameters for stars classified using photometry in Table 1.

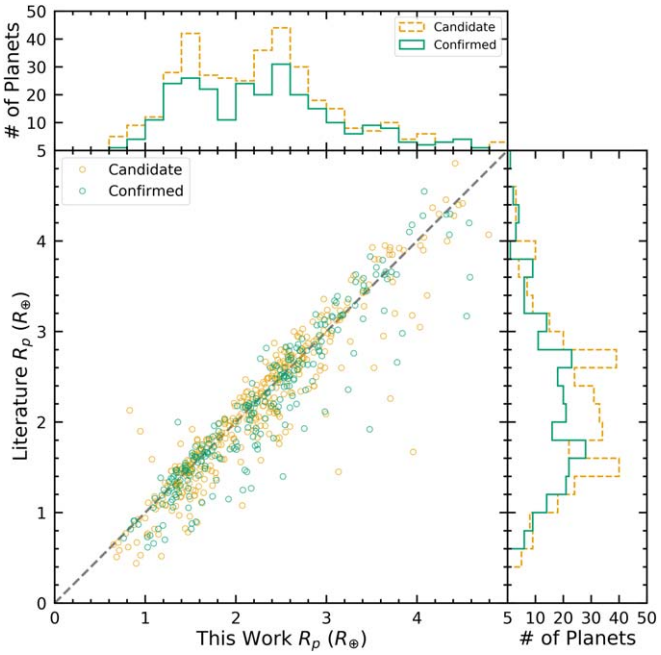

Figure 18. A closer inspection of planets with $R_p < 5\,R_\oplus$ from Figure 17(b) elucidates a planet radius valley around $R_p \approx 1.9\,R_\oplus$ using our updated stellar parameters, which was not present in the previously measured planet radii.

6. Discussion

6.1. Comparison to Previous Stellar Measurements

The EPIC contains $T_{\rm eff}$, log g, [Fe/H], $R_\star$, and $M_\star$ measurements for 192,598 of our targets, which allowed us to compare results. A significant fraction of the stellar properties for these targets in the EPIC were measured using reduced proper motions and colors (165,641), with LAMOST spectra accounting for 8115 targets, RAVE spectra for 4938 targets, APOGEE spectra for 1413 targets, *Hipparcos* parallax for 4912 targets, and colors only for 7579 targets. In Figures 12–14, we compare our $T_{\rm eff}$, log g, [Fe/H], $R_\star$, and $M_\star$ measurements to those from the EPIC, delineating between the different EPIC classification inputs to see if there are any major trends depending on classification method. In general, our effective temperatures are similar regardless of classification method. For surface gravity, there is much more structure, with a few preferential "arms" appearing where there are significant interchanges between dwarfs and giants. There is a positive correlation between the measurements of [Fe/H], but in general our measurements appear to be larger. In the $R_\star$ comparisons, the giant-dwarf interchange arms are again apparent in the reduced proper motion and colors only plots. There are positive correlations between the mass measurements, but our mass measurements are generally larger than EPIC values.

The parameters derived from LAMOST spectra measurements are unsurprisingly similar, with deviations from unity mostly caused by our measurements of M dwarf properties. It is worth noting that our LAMOST measurements are from DR5, whereas the EPIC values come from LAMOST DR1. LAMOST pipeline updates changed computed parameters, and a comparison between LAMOST DR5 and DR3 for the same targets showed a standard deviation of 83 K, 0.13 dex, and 0.07 dex for $T_{\rm eff}$, log g, and [Fe/H], respectively.[15]

[15] http://dr5.lamost.org/doc/release-note-v2

Using our M_{K_s} values, we compare HR diagrams for $T_{\rm eff}$ in the EPIC and our values in Figure 15, showing additional information from surface gravities and radii. The aforementioned giant-dwarf misclassifications are clearly visible in the EPIC HR diagram.

Since there were no M giants in our LAMOST sample, it is difficult to accurately classify these targets for *K2*. M giants will have similar colors to M dwarfs, but very different luminosities. Table 1 contains a few hundred low surface gravity targets ($1.2 \lesssim \log g \lesssim 3.9$) with an assigned M spectral type. Notably, these targets have temperatures higher than ~4200 K, likely due to the random forest regressor assigning temperatures of nearby K giants with similar M_{K_s} magnitudes. We urge caution when using our catalog parameters for targets toward the tip of the giant branch, and recommend using surface gravity and absolute magnitudes to help differentiate between main-sequence and evolved stars.

Gaia measured $T_{\rm eff}$ and $R_\star$ for 174,781 of our stars, which we compare in Figure 16. The *Gaia* temperatures were estimated using G, $G_{\rm BP}$, and $G_{\rm RP}$ colors using a random forest algorithm trained on stars with $T_{\rm eff}$ determined from spectra (Andrae et al. 2018). In general, our $T_{\rm eff}$ measurements are comparable to *Gaia* measurements, but there appear to be more preferential temperatures in the *Gaia* targets, likely caused by their input training set. Our stellar radii correlate well with those determined from *Gaia* which were measured in a manner similar to ours via the Stefan–Boltzmann law, using M_G instead of M_{K_s}. Notably absent from *Gaia* measured radii are stars below $0.5R_\odot$.

6.2. K2 *Planet Hosts and the Planet Radius Valley*

We also compared $R_\star$ measurements for candidate and confirmed planet hosts,[16] using the most recent measurements from the literature for targets with previously measured $R_\star$ and $R_p/R_\star$ (Figure 17(a)). This yielded parameters for 517 candidate and 299 confirmed planets and their hosts for which we also had an $R_\star$ measurement. We do not have new parameters for 375 candidates and 93 confirmed planets, which is due to either lack of previously measured $R_\star$ and $R_p/R_\star$ from the literature, lack of *Gaia* parallaxes, or because the planet hosts do not fall within the color space necessary for our classification. For stars with radii less than $5\,R_\odot$, our $R_\star$ measurements are on average 8.6% and 7.9% larger than literature values for candidate and confirmed planet hosts, respectively. Looking specifically at M dwarfs with radii less than $0.6\,R_\odot$, our measurements are on average 18.5% and 33.3% larger for candidate and confirmed planet hosts. We attribute this significant discrepancy to previous measurements of M dwarf properties using older models that tend to underestimate the radii of cool stars. Using similar measurement techniques, Hardegree-Ullman et al. (2019) and Dressing et al. (2019) also noted that catalog radii for *Kepler* and *K2* M dwarfs were underestimated by ~40–50%.

For proper planet radius measurements, our new stellar properties should be used when fitting the transit light curves, to account for effects such as limb darkening on the transit fit. Refitting transit curves is beyond the scope of this paper, but we offer a general quantitative analysis of updated planet radii R_p based on literature values for $R_p/R_\star$ and our measurements

[16] https://exoplanetarchive.ipac.caltech.edu/cgi-bin/TblView/nph-tblView?app=ExoTbls&config=k2candidates

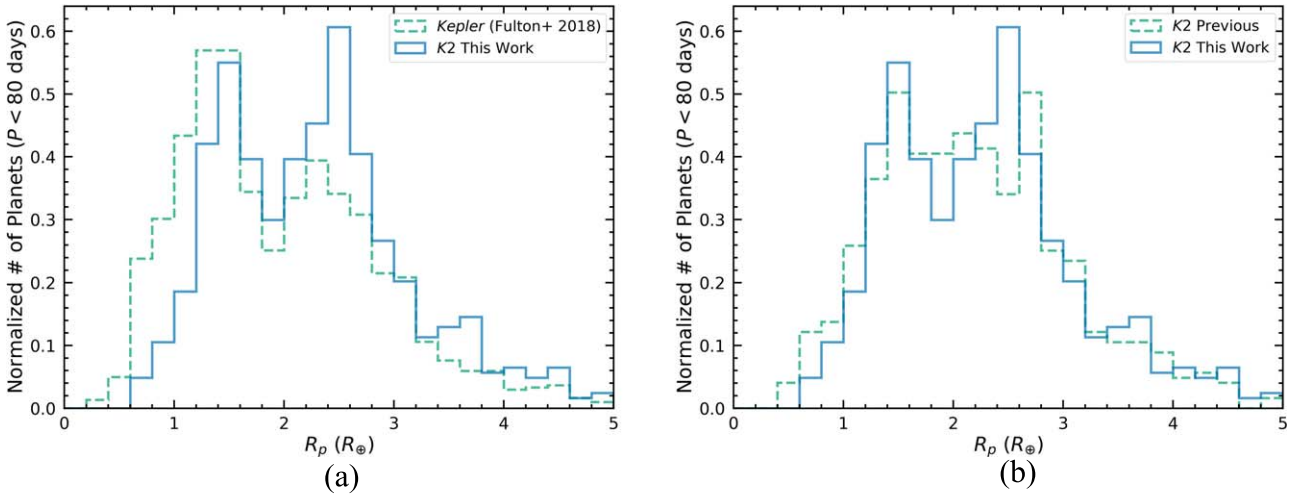

Figure 19. Normalized planet radius distributions for $R_p < 5\,R_\oplus$ and $P < 80$ days for our combined *K2* confirmed and candidate sample, compared to (a) the *Kepler* sample from Fulton & Petigura (2018) and to (b) all previous *K2* measurements. There is a much more prominent valley in our measurements than in previous *K2* measurements. The gap minimum around $R_p \approx 1.9\,R_\oplus$ that we measure is also consistent with the *Kepler* sample. Note that these measurements have not been corrected for completeness.

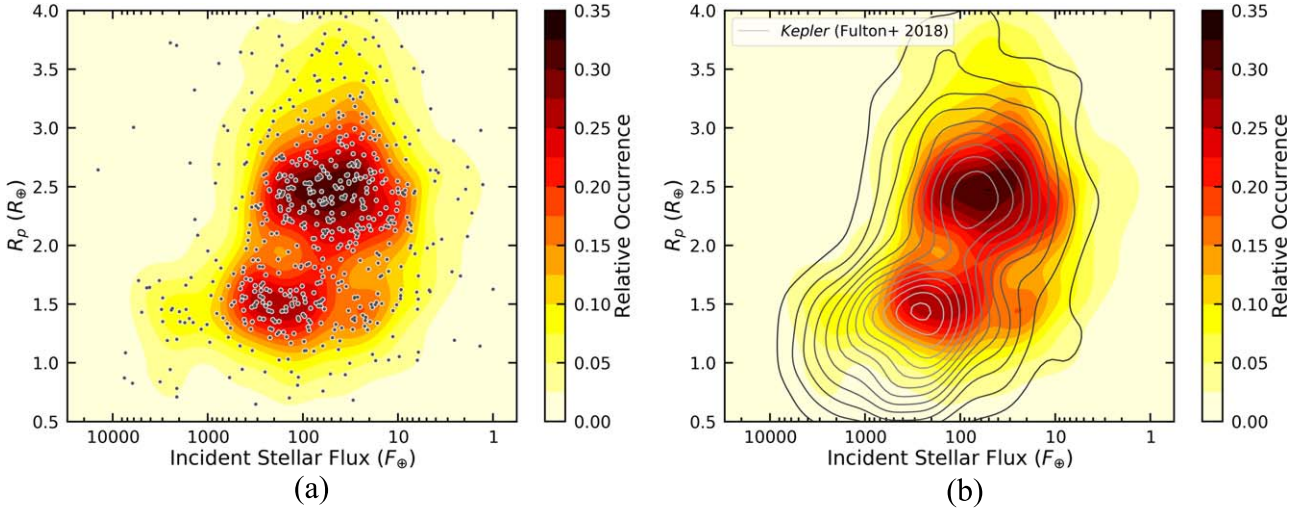

Figure 20. (a) Planet radius vs. incident stellar flux for *K2* planets. Each point is either a confirmed or candidate planet, and the contours show the density of planets. A valley is present around $2\,R_\oplus$, separating a population of super-Earths and sub-Neptunes. (b) The same density contours for *K2* from (a) with the density contours for *Kepler* planets from Fulton & Petigura (2018). The planet populations have similar distributions, with a similar radius gap showing a small slope with respect to incident stellar flux. Note that these plots have not been corrected for completeness.

of $R_\star$. This analysis is valid under the assumption that the change of stellar parameters does not significantly affect the measured transit depth. Table 3 contains our revised planet radii, and Figure 17(b) compares our planet radii to literature values. For planets with $R_p < 20\,R_\oplus$, our planet radii are on average 6.7% and 6.8% larger for candidate and confirmed planets, respectively.

Taking a closer look at planets with $R_p < 5\,R_\oplus$, we investigated the planet radius valley, which is not apparent from previous *K2* planet radii, but is very prominent in our revised radii (Figure 18). The Kruse et al. (2019) measurements constitute about 85% of the previous planet sample, indicating that the differences between our measured stellar radii and the *Gaia* pipeline are not insignificant, and are likely due to the differences in $T_{\rm eff}$. We combined the confirmed and candidate *K2* planet samples, and compared the planet radius distributions from our measurements to the *Kepler* sample from Fulton & Petigura (2018) and all previous *K2* measurements for planets with orbital periods less than 80 days in Figure 19. Our updated stellar and planet radii confirm a distinct planet radius valley with a planet sample other than *Kepler*. This highlights the importance of careful and precise stellar measurements when deriving planet parameters. These measurements were not corrected for completeness, however, which is beyond the scope of this work. Completeness will be addressed in future catalog papers in this series (Zink et al. 2020; J. K. Zink et al. 2020, in preparation).

Using the literature values for orbital period and our computed stellar masses, we calculated semimajor axes a for our set of *K2* planets from Kepler's third law. We then computed incident stellar flux $F_{pl}/F_\oplus = (L_\star/L_\odot)(\mathrm{au}/a)^2$, where stellar luminosity $L_\star/L_\odot = (R_\star/R_\odot)^2(T_{\rm eff}/T_\odot)^4$ computed using our values. In Figure 20, we show planet radius versus incident stellar flux for planets smaller than $4\,R_\oplus$ and orbital periods shorter than 80 days. The density contours show two relatively distinct populations of planets separated by a

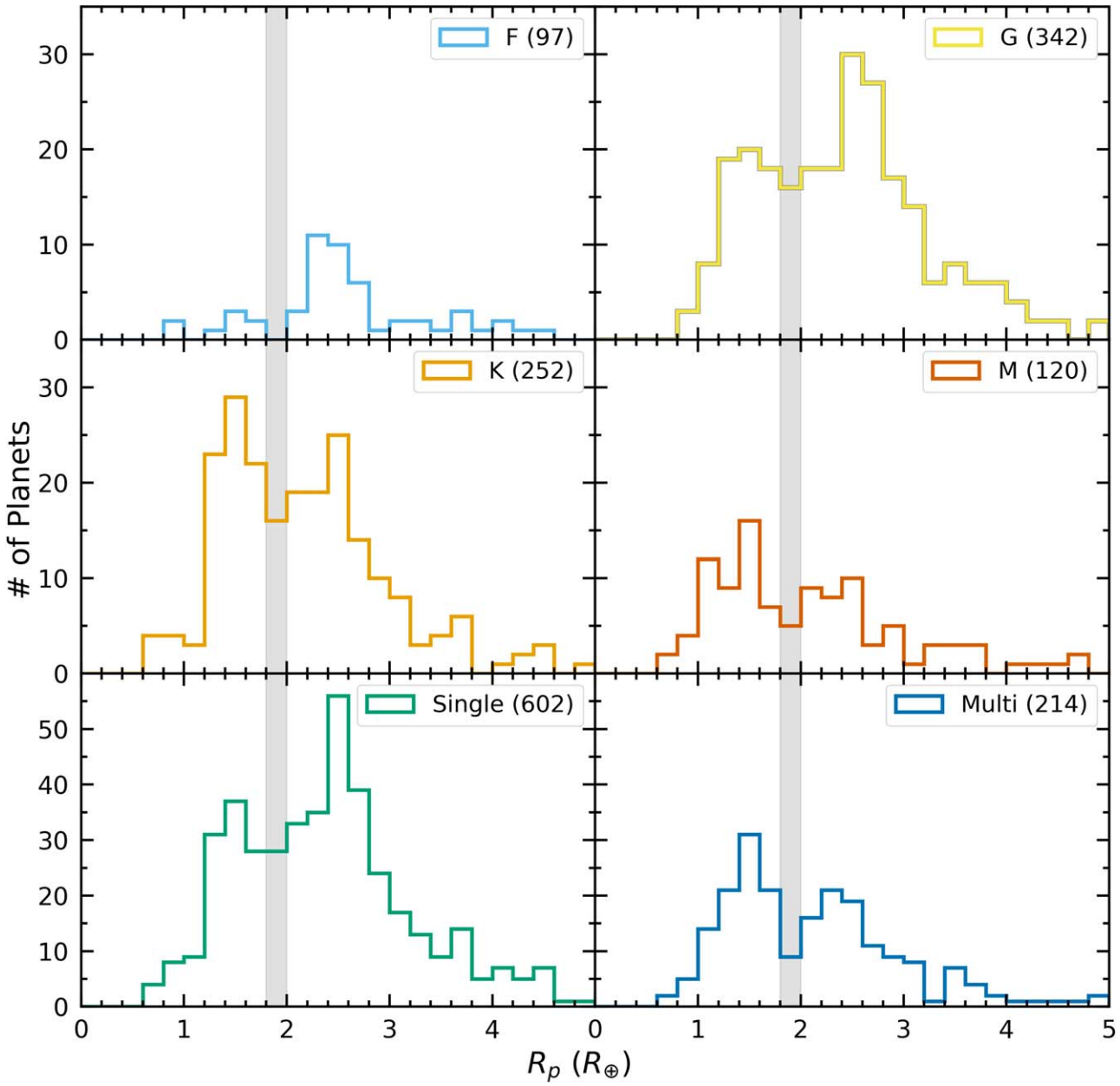

Figure 21. Planet radius distributions separated by spectral type, including both confirmed and candidate planets (top four panels), and single vs. multiple planet systems (bottom two panels). We have shaded the region at 1.9 $R_\oplus$ for reference in comparison to the radius valley of the total sample. For each spectral type, there is evidence for the planet radius valley, which is most prominent for K-type stars. Single planet systems appear to have about twice the fraction of sub-Neptunes compared to super-Earths, whereas the ratio is near unity for multiple planet systems. We again note that these distributions have not been corrected for completeness, so conclusions about planet occurrence rates cannot be drawn from these data.

valley around 2 $R_\oplus$ and a wide range of incident fluxes. As a qualitative comparison, we also show the density contours of the *K2* planet population and the *Kepler* population from Fulton & Petigura (2018). In both cases, the radius valley is apparent at about the same location, with hits of a small slope as a function of incident stellar flux.

Since we have spectral types for all of our stars, we separated the *K2* planet radius distributions by spectral type (Figure 21). For each spectral type, there is a lack of planets at $R_p \approx 1.9\,R_\oplus$. K-type stars show a prominent radius valley, but all other spectral types at least hint at a valley. A larger sample size would be necessary to confirm a valley for F and M stars. Indeed, by combining 275 confirmed *Kepler* and 53 confirmed *K2* K- and M-dwarf planets with host star $T_{\rm eff} < 4700$ K, Cloutier & Menou (2019) showed a more definitive planet valley around 1.54 $R_\oplus$ for planets around cool stars. Further, there is an increasing total fraction of super-Earths ($R_\oplus < R_p < 1.9\,R_\oplus$) to sub-Neptunes ($1.9\,R_\oplus < R_p < 3.86\,R_\oplus$) toward later-type stars, with ratios of 0.20, 0.49, 0.73, and 1.13 for F, G, K, and M stars, respectively, which is consistent with conclusions of planet occurrence rate studies (e.g., Howard et al. 2012; Dressing & Charbonneau 2015; Mulders et al. 2015; Hardegree-Ullman et al. 2019), indicating that smaller planets are more common toward later spectral types. This effect, however, could be an observational bias, since it is more difficult to detect smaller planets around larger stars. We also compared the planet radius distributions for single and multiple planet systems in Figures 21 and 22. There are 602 single planet systems and 90

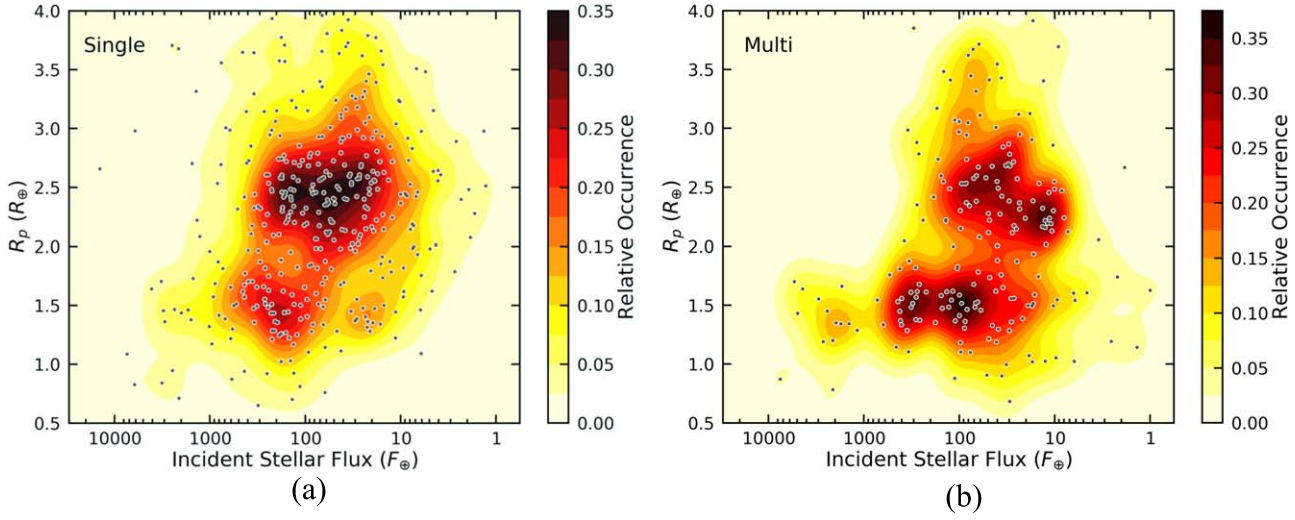

Figure 22. Planet radius vs. incident stellar flux for *K2* planets in single (a) and multiple planet systems (b). Perhaps more evident than in Figure 21, single planet systems appear to have twice as many sub-Neptunes than super-Earths, whereas multiple planet systems have roughly equal numbers of each. Note that these plots have not been corrected for completeness.

multiple planet systems containing a total of 214 planets. For single planet systems, the ratio of super-Earths to sub-Neptunes is 0.51, whereas for multiple-planet systems the ratio is 0.97. We leave the analysis of these effects to future studies (see Weiss et al. 2018 for discussion regarding single versus multiple planet systems in the *Kepler* sample).

6.3. Future Directions

Our uniformly derived catalog of updated stellar parameters for 222,088 *K2* stars using LAMOST spectra, *Gaia* parallaxes, and photometry is a crucial step in the process of calculating *K2* planet occurrence rates. All of the planet candidates analyzed in this paper were from *K2* Campaigns 1–13, since catalogs for those planets have already been made and are available on the Exoplanet Archive. The next step toward computing planet occurrence rates is to develop a pipeline to uniformly process *K2* light curves and automatically identify and vet planet candidates across all campaigns (Zink et al. 2020; J. K. Zink et al. 2020, in preparation). This will enable us to conduct crucial completeness and reliability tests necessary for accurate planet occurrence rate calculations, which we have not been able to account for in this work. With a larger set of planet candidates across all campaigns, a more complete analysis of effects such as the planet radius gap can be assessed. Our large set of $T_{\rm eff}$, log g, [Fe/H], $R_\star$, and $M_\star$ could also enable other statistical population studies of stars and planets.

In this study, we have largely ignored the effects of stellar multiplicity. Duchêne & Kraus (2013) estimate that 44% of all FGK stars are part of a multiple stellar system, and Winters et al. (2019) found a multiplicity rate of ∼27% for M dwarfs within 25 pc of the Sun. *Gaia* is able to resolve binary stars of similar brightness with separations down to about one arcsecond.[17] However, Horch et al. (2014) estimate that 40–50% of planet candidate systems host a bound binary within one arcsecond. Our stellar parameters assume a single star or a wide separation such that we can resolve our target. If the stars are actually in multiple systems, our stellar radii will typically be overestimated, which could have a significant impact on derived planet parameters and conclusions regarding planet populations (e.g., Ciardi et al. 2015; Furlan et al. 2017; Horch et al. 2017; Matson et al. 2018). High-resolution imaging surveys to determine stellar multiplicity rates have largely focused on stars with planet candidates, but it is possible that there are differences in multiplicity rates for hosts versus non-hosts, which could suggest differences in formation mechanisms. We strongly encourage additional high-resolution imaging and high-resolution spectroscopic observations of *K2* stars, including stars without known planets, that enable us to more effectively mitigate and assess the impact of stellar companions on planet occurrence rates.

We thank the anonymous referee for providing several helpful suggestions that improved this manuscript. We would also like to thank Christina Hedges, Geert Barentsen, and Jessie Dotson at the *Kepler* Guest Observer office for constructive discussions about *K2* and this work.

This research has made use of the NASA Exoplanet Archive, which is operated by the California Institute of Technology, under contract with the National Aeronautics and Space Administration under the Exoplanet Exploration Program.

The Pan-STARRS1 Surveys (PS1) and the PS1 public science archive have been made possible through contributions by the Institute for Astronomy, the University of Hawaii, the Pan-STARRS Project Office, the Max-Planck Society and its participating institutes, the Max Planck Institute for Astronomy, Heidelberg and the Max Planck Institute for Extraterrestrial Physics, Garching, The Johns Hopkins University, Durham University, the University of Edinburgh, the Queen's University Belfast, the Harvard–Smithsonian Center for Astrophysics, the Las Cumbres Observatory Global Telescope Network Incorporated, the National Central University of Taiwan, the Space Telescope Science Institute, the National Aeronautics and Space Administration under grant No. NNX08AR22G issued through the Planetary Science Division of the NASA Science Mission Directorate, the National Science Foundation grant No. AST-1238877, the University of Maryland, Eotvos Lorand University (ELTE), the Los Alamos National Laboratory, and the Gordon and Betty Moore Foundation.

[17] https://www.cosmos.esa.int/web/gaia/science-performance

This work has made use of data from the European Space Agency (ESA) mission *Gaia* (https://www.cosmos.esa.int/gaia), processed by the *Gaia* Data Processing and Analysis Consortium (DPAC, https://www.cosmos.esa.int/web/gaia/dpac/consortium). Funding for the DPAC has been provided by national institutions, in particular the institutions participating in the *Gaia* Multilateral Agreement.

This work made use of the gaia-kepler.fun cross-match database created by Megan Bedell. This research made use of the cross-match service provided by CDS, Strasbourg.

Guoshoujing Telescope (the Large Sky Area Multi-Object Fiber Spectroscopic Telescope; LAMOST) is a National Major Scientific Project built by the Chinese Academy of Sciences. Funding for the project has been provided by the National Development and Reform Commission. LAMOST is operated and managed by the National Astronomical Observatories, Chinese Academy of Sciences.

K.H.-U. acknowledges funding from NASA ADAP grant 80NSSC18K0431.

Facilities: Exoplanet Archive, *Gaia*, *Kepler*, LAMOST, PS1.

Software: `astropy` (Astropy Collaboration et al. 2013, 2018), `dustmaps` (Green et al. 2018), `iPython` (Pérez & Granger 2007), `M_-M_K-` (Mann et al. 2019), `matplotlib` (Hunter 2007), `numpy` (Oliphant 2015), `pandas` (McKinney 2010), `scikit-learn` (Pedregosa et al. 2011), `scipy` (Virtanen et al. 2020), `SpectRes` (Carnall 2017).

ORCID iDs

Kevin K. Hardegree-Ullman https://orcid.org/0000-0003-3702-0382
Jon K. Zink https://orcid.org/0000-0003-1848-2063
Jessie L. Christiansen https://orcid.org/0000-0002-8035-4778
Courtney D. Dressing https://orcid.org/0000-0001-8189-0233
David R. Ciardi https://orcid.org/0000-0002-5741-3047
Joshua E. Schlieder https://orcid.org/0000-0001-5347-7062

References

Adams, E. R., Jackson, B., & Endl, M. 2016, AJ, 152, 47
Alam, S., Albareti, F. D., Allende Prieto, C., et al. 2015, ApJS, 219, 12
Andrae, R., Fouesneau, M., Creevey, O., et al. 2018, A&A, 616, A8
Astropy Collaboration, Price-Whelan, A. M., Sipőcz, B. M., et al. 2018, AJ, 156, 123
Astropy Collaboration, Robitaille, T. P., Tollerud, E. J., et al. 2013, A&A, 558, A33
Bailer-Jones, C. A. L., Rybizki, J., Fouesneau, M., Mantelet, G., & Andrae, R. 2018, AJ, 156, 58
Berger, T. A., Huber, D., Gaidos, E., & van Saders, J. L. 2018, ApJ, 866, 99
Bonfils, X., Delfosse, X., Udry, S., et al. 2005, A&A, 442, 635
Borucki, W. J., Koch, D., Basri, G., et al. 2010, Sci, 327, 977
Boyajian, T. S., von Braun, K., van Belle, G., et al. 2012, ApJ, 757, 112
Brown, T. M., Latham, D. W., Everett, M. E., & Esquerdo, G. A. 2011, AJ, 142, 112
Carnall, A. C. 2017, arXiv:1705.05165
Chambers, K. C., Magnier, E. A., Metcalfe, N., et al. 2016, arXiv:1612.05560
Ciardi, D. R., Beichman, C. A., Horch, E. P., & Howell, S. B. 2015, ApJ, 805, 16
Cloutier, R., & Menou, K. 2019, arXiv:1912.02170
Covey, K. R., Ivezić, Ž, Schlegel, D., et al. 2007, AJ, 134, 2398
Crossfield, I. J. M., Ciardi, D. R., Petigura, E. A., et al. 2016, ApJS, 226, 7
Cui, X.-Q., Zhao, Y.-H., Chu, Y.-Q., et al. 2012, RAA, 12, 1197
Cushing, M. C., Marley, M. S., Saumon, D., et al. 2008, ApJ, 678, 1372
Dawson, K. S., Schlegel, D. J., Ahn, C. P., et al. 2013, AJ, 145, 10
Dotter, A. 2016, ApJS, 222, 8
Dressing, C. D., & Charbonneau, D. 2015, ApJ, 807, 45
Dressing, J. E., Hardegree-Ullman, C. D., Schlieder, K., et al. 2019, AJ, 158, 87
Dressing, J. E., Newton, C. D., Schlieder, E. R., et al. 2017a, ApJ, 836, 167
Dressing, J. E., Vanderburg, C. D., Schlieder, A., et al. 2017b, AJ, 154, 207
Duchêne, G., & Kraus, A. 2013, ARA&A, 51, 269
Evans, D. W., Riello, M., De Angeli, F., et al. 2018, A&A, 616, A4
Flewelling, H. A., Magnier, E. A., Chambers, K. C., et al. 2016, arXiv:1612.05243
Fulton, B. J., & Petigura, E. A. 2018, AJ, 156, 264
Fulton, B. J., Petigura, E. A., Howard, A. W., et al. 2017, AJ, 154, 109
Furlan, E., Ciardi, D. R., Everett, M. E., et al. 2017, AJ, 153, 71
Gaia Collaboration, Brown, A. G. A., Vallenari, A., et al. 2018, A&A, 616, A1
Gaia Collaboration, Prusti, T., de Bruijne, J. H. J., et al. 2016, A&A, 595, A1
Girardi, L., Bressan, A., Bertelli, G., & Chiosi, C. 2000, A&AS, 141, 371
Green, G. M., Schlafly, E. F., Finkbeiner, D., et al. 2018, MNRAS, 478, 651
Hardegree-Ullman, K. K., Cushing, M. C., Muirhead, P. S., & Christiansen, J. L. 2019, AJ, 158, 75
Horch, E. P., Casetti-Dinescu, D. I., Camarata, M. A., et al. 2017, AJ, 153, 212
Horch, E. P., Howell, S. B., Everett, M. E., & Ciardi, D. R. 2014, ApJ, 795, 60
Howard, A. W., Marcy, G. W., Bryson, S. T., et al. 2012, ApJS, 201, 15
Howell, S. B., Rowe, J. F., Bryson, S. T., et al. 2012, ApJ, 746, 123
Howell, S. B., Sobeck, C., Haas, M., et al. 2014, PASP, 126, 398
Huber, D., Bryson, S. T., Haas, M. R., et al. 2016, ApJS, 224, 2
Hunter, J. D. 2007, CSE, 9, 90
Husser, T. O., Wende-von Berg, S., Dreizler, S., et al. 2013, A&A, 553, A6
Johnson, J. A., & Apps, K. 2009, ApJ, 699, 933
Kesseli, A. Y., West, A. A., Veyette, M., et al. 2017, ApJS, 230, 16
Kirkpatrick, J. D., Henry, T. J., & McCarthy, D. W., Jr. 1991, ApJS, 77, 417
Koleva, M., Prugniel, P., Bouchard, A., & Wu, Y. 2009, A&A, 501, 1269
Kordopatis, G., Gilmore, G., Steinmetz, M., et al. 2013, AJ, 146, 134
Kruse, E., Agol, E., Luger, R., & Foreman-Mackey, D. 2019, ApJS, 244, 11
Lee, E. J., & Chiang, E. 2016, ApJ, 817, 90
Lee, E. J., Chiang, E., & Ormel, C. W. 2014, ApJ, 797, 95
Lopez, E. D., & Rice, K. 2018, MNRAS, 479, 5303
Luo, A. L., Zhang, H.-T., Zhao, Y.-H., et al. 2012, RAA, 12, 1243
Luo, A. L., Zhao, Y.-H., Zhao, G., et al. 2015, RAA, 15, 1095
Mamajek, E. E., Torres, G., Prsa, A., et al. 2015, arXiv:1510.06262
Mann, A. W., Brewer, J. M., Gaidos, E., Lépine, S., & Hilton, E. J. 2013a, AJ, 145, 52
Mann, A. W., Deacon, N. R., Gaidos, E., et al. 2014, AJ, 147, 160
Mann, A. W., Dupuy, T., Kraus, A. L., et al. 2019, ApJ, 871, 63
Mann, A. W., Feiden, G. A., Gaidos, E., Boyajian, T., & von Braun, K. 2015, ApJ, 804, 64
Mann, A. W., Gaidos, E., & Ansdell, M. 2013b, ApJ, 779, 188
Mann, A. W., Gaidos, E., Vanderburg, A., et al. 2017, AJ, 153, 64
Marigo, P., & Girardi, L. 2007, A&A, 469, 239
Marigo, P., Girardi, L., Bressan, A., et al. 2008, A&A, 482, 883
Martinez, A. O., Crossfield, I. J. M., Schlieder, J. E., et al. 2017, ApJ, 837, 72
Matson, R. A., Howell, S. B., Horch, E. P., & Everett, M. E. 2018, AJ, 156, 31
Mayo, A. W., Vanderburg, A., Latham, D. W., et al. 2018, AJ, 155, 136
McKinney, W. 2010, in Proc. 9th Python in Science Conf., ed. S. van der Walt & J. Millman (Austin, TX: SciPy), 51
Morton, T. D. 2015, Isochrones: Stellar Model Grid Package v.2.0.1, Astrophysics Source Code Library, ascl:1503.010
Muirhead, P. S., Mann, A. W., Vanderburg, A., et al. 2015, ApJ, 801, 18
Mulders, G. D., Pascucci, I., & Apai, D. 2015, ApJ, 814, 130
Neves, V., Bonfils, X., Santos, N. C., et al. 2012, A&A, 538, A25
Newton, E. R., Charbonneau, D., Irwin, J., et al. 2014, AJ, 147, 20
Oliphant, T. E. 2015, Guide to NumPy
Osborn, H. P., Armstrong, D. J., Brown, D. J. A., et al. 2016, MNRAS, 457, 2273
Owen, J. E., & Wu, Y. 2013, ApJ, 775, 105
Owen, J. E., & Wu, Y. 2017, ApJ, 847, 29
Pedregosa, F., Varoquaux, G., Gramfort, A., et al. 2011, J. Mach. Learn. Res., 12, 2825
Pérez, F., & Granger, B. E. 2007, CSE, 9, 21
Petigura, E. A., Crossfield, I. J. M., Isaacson, H., et al. 2018, AJ, 155, 21
Rojas-Ayala, B., Covey, K. R., Muirhead, P. S., & Lloyd, J. P. 2010, ApJL, 720, L113
Rojas-Ayala, B., Covey, K. R., Muirhead, P. S., & Lloyd, J. P. 2012, ApJ, 748, 93
Schlaufman, K. C., & Laughlin, G. 2010, A&A, 519, A105
Sharma, S., Bland-Hawthorn, J., Johnston, K. V., & Binney, J. 2011, ApJ, 730, 3
Skrutskie, M. F., Cutri, R. M., Stiening, R., et al. 2006, AJ, 131, 1163

Terrien, R. C., Mahadevan, S., Bender, C. F., et al. 2012, ApJL, 747, L38
Terrien, R. C., Mahadevan, S., Deshpande, R., & Bender, C. F. 2015, ApJS, 220, 16
Van Eylen, V., Agentoft, C., Lundkvist, M. S., et al. 2018, MNRAS, 479, 4786
van Leeuwen, F. 2007, A&A, 474, 653
Virtanen, P., Gommers, R., Oliphant, T. E., et al. 2020, Nature Methods, 17, 261
Weiss, L. M., Isaacson, H. T., Marcy, G. W., et al. 2018, AJ, 156, 254
Winters, J. G., Henry, T. J., Jao, W.-C., et al. 2019, AJ, 157, 216
Woolf, V. M., Lépine, S., & Wallerstein, G. 2009, PASP, 121, 117
Wu, Y., Luo, A. L., Li, H.-N., et al. 2011, RAA, 11, 924
Yi, Z., Luo, A., Song, Y., et al. 2014, AJ, 147, 33
Zacharias, N., Finch, C. T., Girard, T. M., et al. 2013, AJ, 145, 44
Zink, J. K., Hardegree-Ullman, K. K., Christiansen, J. L., et al. 2019, RNAAS, 3, 43
Zink, J. K., Hardegree-Ullman, K. K., Christiansen, J. L., et al. 2020, AJ, submitted (arXiv:2001.11515)